

Institut für Schichten und Grenzflächen

# STM studies of islands on Cu and Pt surfaces

Julian Borislavov Ikonomov

# STM studies of islands on Cu and Pt surfaces

Julian Borislavov Ikonomov

Berichte des Forschungszentrums Jülich ; 4144 ISSN 0944-2952 Institut für Schichten und Grenzflächen Jül-4144 D 61 (Diss., Düsseldorf, Univ., 2004)

Zu beziehen durch: Forschungszentrum Jülich GmbH · Zentralbibliothek D-52425 Jülich · Bundesrepublik Deutschland ☎ 02461 61-5220 · Telefax: 02461 61-6103 · e-mail: zb-publikation@fz-juelich.de

#### **Abstract**

This thesis deals with quantitative studies of equilibrium and non-equilibrium phenomena on Pt(111) and Cu(100) surfaces using scanning tunneling microscopy (STM). The aim of this work is apply theoretical methods based on statistical physics to determine atomistic energy parameters of surface diffusion processes on metal substrates which cannot be directly detected, and hence, analyzed as individual atomic hopping events. As was shown previously, one may determine activation barriers of diffusion, pre-exponential factors and formation energies. In this thesis, the theoretical methods were applied to Pt(111) and Cu(100) substrates and step free energies were measured, dominant mass transport processes were identified and the relevant activation energies were obtained. On Pt(111), for instance, the equilibrium shape and the equilibrium edge fluctuations of monatomic high islands were studied between 533 K and 713 K. Using the measured equilibrium shapes, the ratio between the step free energies of A- and B-steps on Pt(111) was analyzed for the first time as a function of temperature. Using the relatively new method of island edge fluctuation studies, absolute values for the free energies for A- and B-steps on Pt(111) could be determined experimentally for the first time.

As a non-equilibrium phenomena, the Ostwald ripening of single-layer deep vacancy islands on Cu(100) was investigated between 323 K and 398 K. A previous result could be confirmed that the mono-vacancies are the dominant mass transport species on Cu(100). From the temperature dependence of the decay rate, the relevant activation energy have been obtained. Comparing the activation energy found in this thesis with previous measurements allowed the determination of the sticking barrier of mono-vacancies at vacancy island edges on Cu(100). A further island decay process was studied in this work which has been discovered only recently to accelerate island decay on fcc(111) surfaces, the rapid island decay. In this thesis, it is shown that this fast decay channel exists also on Pt(111). Finally, a coarsening process is discussed which has a great importance on fcc (100) surfaces, the island coalescence. Here, the

coalescence of single-layer deep vacancy islands on Cu(100) was investigated between 303 K and 353 K. It could be shown that the equilibration of the island shape after coalescence is dominated by atom diffusion along the island edges. The relevant activation energy was determined and the result corroborates recent preliminary studies of fluctuations of highly-kinked steps which showed that the activation energy is much lower compared to the energy measured for steps along the atomically dense direction.

## Kurzfassung

Im Rahmen dieser Doktorarbeit wurden Gleichgewichtsund Nicht-Gleichgewichtsphänomene auf Pt(111)- und Cu(100)-Oberflächen mittels eines Rastertunnelmikroskops (RTM) quantitativ untersucht. Das Ziel dieser Arbeit war, theoretische Methoden, die auf der statistischen Physik basieren, bei der Analyse von RTM-Bildern anzuwenden und dadurch atomistische Energieparameter Oberflächendiffusion auf Metallsubstraten zu bestimmen. Hier wurde insbesondere auf solche Prozesse das Augenmerk gelegt, bei welchen die individuellen atomaren Hüpfprozesse nicht direkt beobachtet und somit auch bezüglich der Energieparameter nicht unmittelbar ausgewertet werden können. Wie früher bereits gezeigt wurde, kann mittels dieser theoretischen Methoden man Aktivierungsenergien die Oberflächendiffusion, prä-exponentielle Faktoren sowie Bildungsenergien bestimmen. In dieser Arbeit wurden die theoretischen Methoden angewendet, um freie Stufenenergien zu messen, dominante Transportprozesse auf den Oberflächen zu identifizieren sowie die relevanten Diffusionsbarrieren zu ermitteln. Für Pt(111) wurde Gleichgewichtsform von monoatomar hohen Adatominseln Randfluktuationen in einem Temperaturbereich zwischen 533 und 713 K gemessen. Daraus konnte erstmalig das Verhältnis zwischen den freien Energien von sogenannten A- und B-Stufen auf Pt(111) als Funktion der Temperatur ermittelt werden. Durch Anwendung der relativ neuen Methode der Analyse der Inselrandfluktuationen konnten zudem erstmalig experimentelle Werte für die absoluten Stufenenergien für A- und B-Stufen angegeben werden ( $\beta_A = 395 \pm 17 \text{ meV}$ ,  $\beta_B = 340 \pm 17 \text{ meV}$ ).

Als Beispiel für ein Nicht-Gleichgewichtsphänomen wurde die Ostwald-Reifung von monoatomar hohen Leerstelleninseln auf Cu(100) wurde zwischen 323K und 398K untersucht. Hier konnte ein früheres Ergebnis bestätigt werden, daß auf Cu(100) monoatomare Leerstellen die dominante Transportspezies darstellen. Durch Messung der temperaturabhängigen Zerfallsrate erhält man die relevante Aktivierungsenergie. Der Vergleich mit den früheren Messungen erlaubte erstmalig auch die direkte Messung der Anlagerungsbarriere von Leerstellen an den Rand einer Leerstelleninsel auf Cu(100)

zu etwa 0.1 eV. In dieser Arbeit wurde ein weiterer Zerfallsprozess untersucht, der erst kürzlich als ein wichtiger Prozess auf fcc(111) Flächen entdeckt wurde und der den Inselzerfall erheblich beschleunigen kann, der schnelle Inselzerfall. Hier konnte gezeigt werden, daß ein solcher Prozess auch auf Pt(111) existiert. Schließlich wurde ein weiterer Reifungsprozeß untersucht, der insbesondere auf fcc (100) Flächen eine wichtige Rolle spielt, die Inselkoaleszenz. Sie wurde im Rahmen dieser Arbeit für den Fall monoatomar hoher Leerstelleninseln auf Cu(100) zwischen 303K und 353K untersucht. Es konnte gezeigt werden, daß die Equilibrierung der Inselform nach der Koaleszenz vorwiegend durch Diffusion entlang der Inselkanten getragen wird. Die Aktivierungsenergie konnte zu 614 meV bestimmt werden. Der zugehörige präexponentielle Faktor ist etwa 10<sup>14</sup> s<sup>-1</sup>. Während letzterer in der erwarteten Größenordnung liegt, ist die Aktivierungsenergie von 614 meV deutlich kleiner als man es für die Diffusion entlang von Stufen, die im Mittel entlang der atomar dichten Richtung verlaufen, kennt. Dieses Ergebnis bestätigt jedoch eine kürzliche, vorläufige Analyse von Stufenfluktuationen stark gekinkter Stufen, bei der ebenfalls eine Aktivierungsenergie von etwa 650 meV gemessen wurde.

## **Contents**

1.	Introd	luction	1	
2.	Island	s on the crystal surface		
3.	Exper	rimental Set Up	9	
	3.1	The UHV-Chamber	9	
	3.2	Sample preparation	11	
	3.3	The STM	12	
	3.4	Processing the STM-images	14	
4.	Island	ls in equilibrium	17	
	4.1	Equilibrium island shape	17	
	4.2	Wulff construction	18	
	4.3	Island shape fluctuations	23	
	4.4	Determination of the step free energies on Pt(111) surface	29	
5.	Non-e	quilibrium phenomena	39	
	5.1	Island decay	39	
		5.1.1 Chemical potential of two-dimensional islands	39	
		5.1.2 Theory of Ostwald ripening	42	
		5.1.3 Island decay on Cu(100)	49	
		5.1.4 Rapid island decay	58	
	5.2	Island coalescence on Cu(100)	64	
		5.2.1 Introduction to island coalescence and theoretical		
		aspects	64	

	5.2.2	Determination of the dominant mass transport		
		mechanism by analyzing the island coal	lescence on	
		Cu(100)	70	
6.	Summary and	l outlook	77	
Refe	erences		81	
Ack	nowlegments			

## Figures and tables

Figure 2.1	TSK model of the crystal surface.	5
Figure 2.2	Models of adatom and vacancy islands of fcc metals.	6
Figure 2.3	Schematic representation of the energy barriers for an	
	adatom close to the step.	8
Figure 3.1.1	The schematics of the UHV-chamber.	9
Figure 3.3.1	Schematic drawing of the STM.	12
Figure 3.4.1	Detection of the island perimeter.	14
Figure 3.4.2	One-dimensional cross section of a vacancy island.	15
Figure 4.2.1	Wulff construction.	19
Figure 4.2.2	Inverse Wulff construction.	21
Figure 4.2.3	Extrema in the step free energy of islands on fcc(100) and	
	fcc(111) surfaces.	22
Figure 4.3.1	Equilibrium shape and real island perimeter.	23
Figure 4.4.1	STM-image of the Pt(111) surface at 633K.	29
<b>Table 4.4.1</b>	The number of islands used to determine the equilibrium	
	shape for a given temperature.	30
Figure 4.4.2	Measured equilibrium shapes for $Pt(111)$ .	30
Figure 4.4.3	The ratio of the radii for A- and B-steps in equilibrium	
	shapes on Pt(111) vs. temperature.	31
Figure 4.4.4	Wulff-plot $\beta(\theta)$ for $Pt(111)$	32
Figure 4.4.5	The time averaged fluctuation function vs. the product of the	
	mean island radius and temperature.	33
Figure 4.4.6	Plot of $\beta(\theta)/\beta(0^\circ)$ and $r(\theta)/r(0^\circ)$ at 633 K	35
<b>Table 4.4.1</b>	Experimental and theoretical data for the step free energies	
	on Pt(111).	36
Figure <b>5.1.2.1</b>	Schematic representation of the island configuration used to	
	derive the Ostwald theory.	42

<b>Figure 5.1.2.2</b>	Illustration to the derivation of the decay equations.	44
<b>Figure 5.1.2.3</b>	Model of the energy barrier for the sticking of an adatom at	
	an island edge.	45
Figure 5.1.3.1	Typical STM-image of the Cu(100) surface at 323K	49
Figure 5.1.3.2	The evolution of vacancy islands on Cu(100) with time at	
	353K.	50
Figure 5.1.3.3	Decay curves of vacancy islands on Cu(100) at 353K.	51
<b>Table 5.1.3.1</b>	Decay exponent for vacancy island decay on Cu(100) at	
	T=323K.	53
<b>Table 5.1.3.2</b>	Decay exponent for vacancy island decay on Cu(100) at	
	T=353K.	53
<b>Table 5.1.3.3</b>	Decay exponent for vacancy island decay on Cu(100) at	
	T=363K.	54
<b>Table 5.1.3.4</b>	Decay exponent for vacancy island decay on Cu(100) at	
	T=398K.	54
Figure 5.1.3.4	Arrhenius plot of $dA/dt _{A^*}$ for vacancy islands at	
	temperatures between 323K and 398K.	56
<b>Figure 5.1.4.1</b>	STM-image of a Pt(111) surface at 513K.	59
<b>Figure 5.1.4.2</b>	STM-images of an adatom island on Pt(111) surface at	
	353K.	60
Figure 5.1.4.3	Decay curve of the adatom island on Pt(111) demonstrating	
	the effect of the rapid island decay.	61
<b>Figure 5.1.4.4</b>	Distance between the island and the step edge during the	
	rapid island decay.	62
Figure 5.1.4.5	Model of the microscopic process during rapid island decay.	63
<b>Figure 5.2.1.1</b>	The dynamic coalescence of two vacancy islands on Cu(100)	
	at 323K.	65
Figure 5.2.1.2	Schematic presentation of the nomenclature used for the	
	definition of the correlation function and for the diffusion	
	processes involved in the relaxation of an island after	
	coalescence.	67

Figure 5.2.2.1	Definition of the measured neck width d and the cluster		
	length h.	70	
<b>Figure 5.2.2.2</b>	Time dependence of the neck width d and the largest		
	diameter of the cluster h for the coalesce vacancy islands on		
	Cu(100) at 323K.	<b>7</b> 1	
Figure 5.2.2.3	Log-log plot of the relaxation time vs. cluster area.	72	
<b>Figure 5.2.2.4</b>	Arrhenius plot of the normalized relaxation time.	73	

Introduction 1

## Chapter 1

#### Introduction

During the last two decades, surface science became one of the fastest developing topics in physics. The interest in this area is provoked by the ceaseless necessity of further miniaturization in microelectronics, new mechanisms in catalysis, the protection against corrosion etc. All these fields of scientific interest still hold a lot of unanswered questions in physics of surfaces which have to be solved. To find a deep understanding of the aforementioned scientific areas, to understand the basic driving forces and atomic processes involved, one has to take a close look to the nano-scale physics of surfaces. Since the invention of the Field Ion Microscope (FIM) [1], which is capable to provide atomically resolved images, scientists are able to observe the motion of individual atoms. Due to the use of strong electric fields in the FIM, the studies, however, are limited to samples of materials of large cohesive energy such as iridium, tungsten and platinum. With the development of the Scanning Tunneling Microscope (STM) [2, 3], the direct observation of nano-structures on a large variety of conducting and semi-conducting surfaces became possible. STM allows not exclusively the observation and analysis of crystal surfaces, but provides techniques to form and manipulate massive nano-structures. However, besides all progress made in recent years, we are still far from nano-devices production on an industrial scale using the STM as a manipulation instrument. The STM is nevertheless a very helpful tool to study the atomistic aspects in nanostructure growth, stability and manipulation.

Many scientific problems of the atomistic details of the dynamics of nanostructures on surfaces are still unsolved. During the last years much work has been, therefore, focused on studies of one- and two-dimensional nanostructures, such as steps and islands, and their behavior under different thermodynamic conditions. Steps and islands are of special interest in surface science, since they are preferred sites for

chemical reactions in catalysis and they frequently serve as the starting sites in corrosion. It has been shown in previous studies [4-9] that the analysis of step fluctuations provides information on surface mass transport mechanisms and the activation energies of diffusion. The equilibrium shape of the islands follows the principle of Helmholtz free energy minimization. Hence, the Helmholtz free energy of steps may be determined by an analysis of island edge fluctuations around the equilibrium shape [4-9]. The part of this work concerning equilibrium shapes of islands and island fluctuations was provoked by the previous work in our group that addressed studies of island fluctuations on Cu(111) and Ag(111) [6, 7, 9]. Choosing Pt(111) now as a sample was a straight-forward consequence in two aspects: First of all, to apply a relatively new method to measure step free energies to a material with large cohesive energy. And second, to apply the method to a material that has, in contrast to Cu(111) and Ag(111), a significant difference in the step free energies for so called A- and B-steps which form the island perimeter on fcc(111) surfaces.

Since the existence of islands on surfaces represents a non-equilibrium state of the surface, island studies may also involve the analysis of non-equilibrium phenomena. Island decay and island coalescence are such phenomena and a detailed analysis may provide insight into the underlying atomic processes, such as terrace and edge diffusion. Other non-equilibrium phenomena, such as e.g. the so-called fast island decay [10] may involve exchange processes and are yet not fully understood.

The present work deals with the investigation of islands on metal surfaces. It is divided in two main topics: First, the investigation of islands in equilibrium which involves the analysis of the equilibrium island shape and shape fluctuations on Pt(111). Second, studies of islands far from equilibrium, which consider normal island decay on Cu(100) and fast island decay on Pt(111) as well as island coalescence on Cu(100). The thesis is organized as follows: After the introduction, Chapter 2 will provide a description of the basics on crystal surfaces, the two-dimensional surface structures and the relevant energetic limits. This chapter is followed by a description of the experimental set-up in chapter 3. In Chapter 4, the theoretical description of the Wulff construction and of the equilibrium island shape is given. This is followed by the theory of island edge fluctuations. At the end of Chapter 4, the experimental results on the equilibrium island shape and island shape fluctuations on Pt(111) are discussed. Chapter

Introduction 3

5 starts with the description of the classical theory of Ostwald ripening, followed by the experimental results on island decay on Cu(100). Subsequently, the experimental findings on rapid island decay on Pt(111) are presented. At the end of Chapter 5, the theory and experimental results for dynamic island coalescence on Cu(100) will be presented. The thesis ends with a summary and outlook in Chapter 6.

4\_\_\_\_\_Chapter 1

## Islands on the crystal surface

In order to describe the crystal surface and its dynamic and kinetic surface processes such as growth and coarsening, one must use an appropriate model. A frequently used representation of crystal surfaces is the Terrace-Step-Kink (TSK) model, which was first described by Burton, Carbrera and Frank [11]. In this model, a crystal is assembled of cubes and the crystal surface consists of terraces, monolayer high steps, kinks at steps, adatom and vacancy islands, as well as single adatoms and mono-vacancies. It is assumed that the interaction is only between the next neighbors. A model of a crystal surface containing defects on the nano-scale relevant for the studies presented in this thesis is shown on Fig. 2.1. The figure shows a surface with a

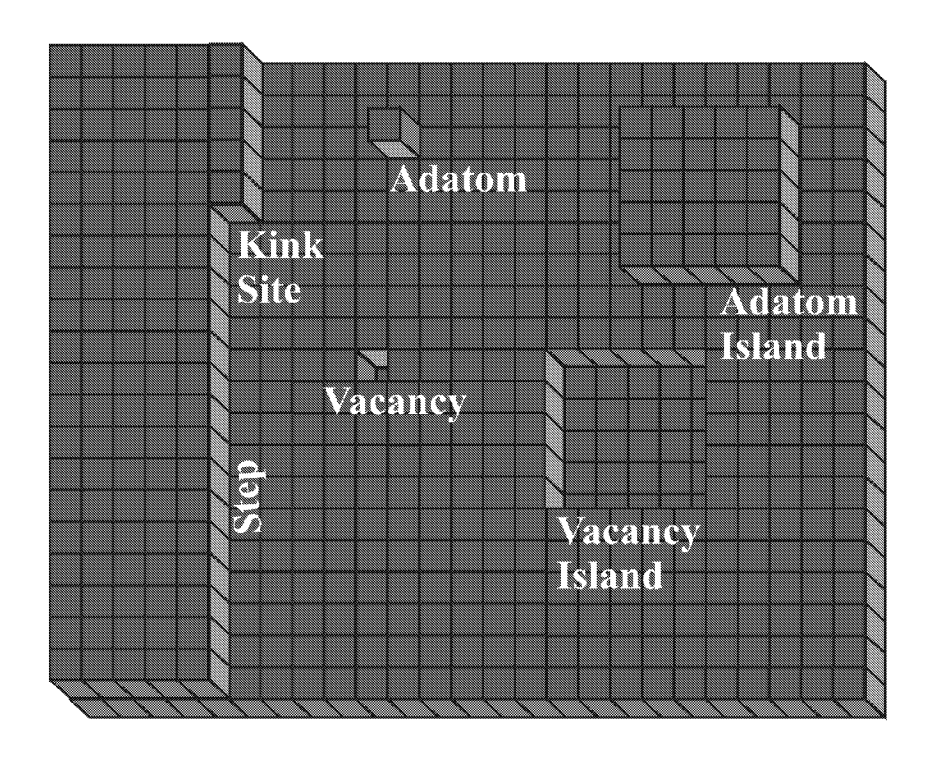
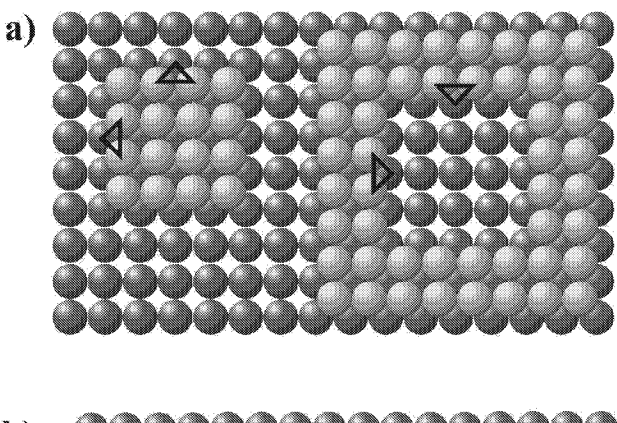


**Figure 2.1** *TSK model of the crystal surface and characteristic nanostructures. The atoms are presented as cubes.* 

monoatomic high step, a kink site, single adatoms and vacancies as well as adatom and vacancy islands. Although the TSK model is a quite simple description of surfaces it provides a good description of surface properties in most cases. This is in particular the case for simple fcc metal surfaces.

Adatom and vacancy islands can be created on surfaces by deposition and removing surface atoms, respectively. Monolayer high islands are produced, if the deposition is stopped before nucleation of the second layer sets in. In the models shown in the following, exclusively monolayer islands are shown, multilayer adatom and vacancy islands may be represented by similar models, however, with further layers added, respectively, removed. The general conclusions drawn in the following are not altered though.

In Fig. 2.2, models of islands on (100) and (111) surfaces of fcc metals are shown. The islands on (100) surfaces are quadratic in shape and the island perimeter consists of step segments of (111) orientation (Fig. 2.2a). The picture is completely different for islands on (111) surfaces (Fig. 2.2b). Due to the trigonal symmetry of the surface, the island perimeter consists of two sets of alternating steps revealing (100)-



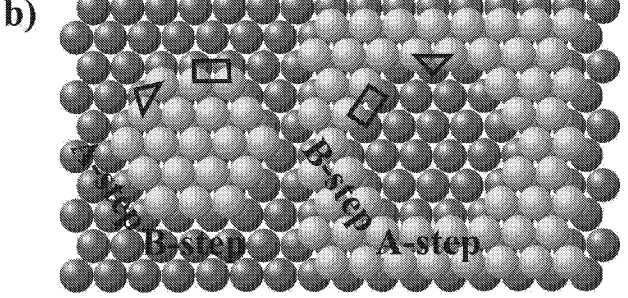


**Figure 2.2** Models of adatom and vacancy islands of fcc metals on a a) (100) and b) (111) surface. The different step facets are indicated.

and (111)-microfacets. These two sets of steps are called A- and B-steps, respectively. Due to the different coordination of the atoms in A- and B-steps, the steps may have different step free energies. According to the difference in step free energy, island edge segments with A- and B-orientation have a different total length, as e.g. is the case for Pt(111) where the islands have a trigonal shape. If A- and B-steps have about the same step free energy, the island equilibrium shape is close to a hexagon, as e.g. is the case for Cu(111). In this thesis, adatom and vacancy islands with monoatomic height, respectively, depth were considered. For Cu(100), the island decay and island coalescence of vacancy islands with monolayer depth were studied. Adatom and vacancy islands with multilayer height/depth were analyzed in the studies of fast island decay on Pt(111).

At temperatures above T = 0 K, crystal surfaces are not static [12]. Adatoms and vacancies diffuse on the surface, they attach and detach at steps and steps as well as islands undergo equilibrium fluctuations. All of these dynamic processes involve single or multiple atomic processes. Each individual process has a specific activation barrier. In Fig. 2.3, the energy barriers of an adatom close to the step are shown. The equilibrium concentration of adatoms on the terrace is determined by the adatom formation energy E<sub>ad</sub>. The annihilation of an adatom by attachment of the adatom from the terrace to the step has an activation energy Eatt. For diffusion of the adatom on the terrace it has to overcome the diffusion barrier  $E_{diff}$ . When an adatom approaches a step from the upper terrace it frequently has to overcome an additional activation barrier E<sub>es</sub>, which is called Ehrlich-Schwoebel barrier [13, 14]. All activation energies mentioned here and shown in Fig. 2.3 exist also for single vacancies. The single atomic events mentioned above cannot be observed directly with the contemporary STM-techniques in most cases. Atomic processes with high activation energies occur only at higher surface temperatures. In order to study coarsening phenomena such as island decay and coalescence these processes have to occur with a high statistical probability which requires also high temperatures. For example for Pt(111), island decay can be observed only at temperatures above 600 K. At such high temperatures, the STM has an insufficient time resolution for all atomic processes relevant for surface coarsening.

In order to obtain information on the dominant atomic transport events one has to choose indirect methods to study the time and temperature dependence of the

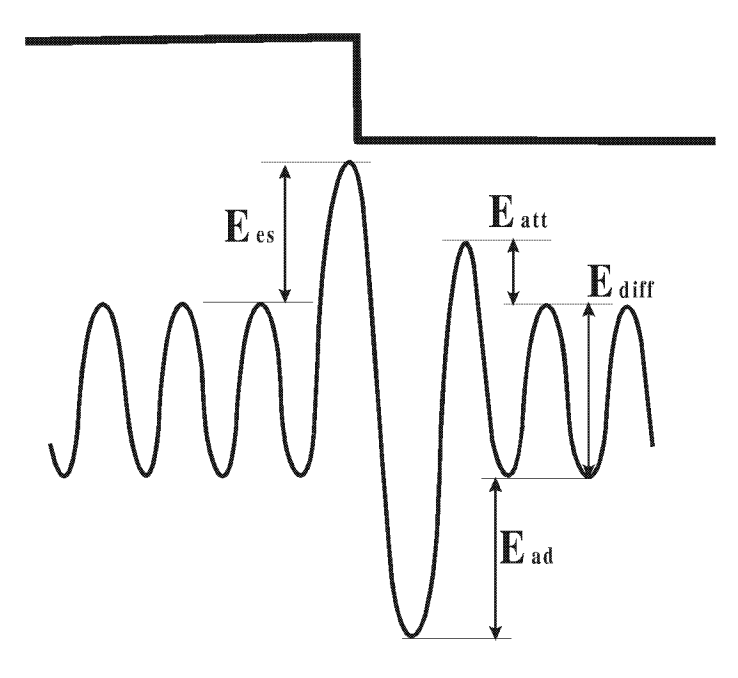


**Figure 2.3** Schematic representation of the energy barriers for an adatom close to the step.  $E_{ad}$  is the adatom formation energy on the terrace,  $E_{es}$  is the Ehrlich-Schwoebel barrier,  $E_{att}$  is the adatom attachment energy at a step and  $E_{diff}$  is the diffusion barrier on the terrace. Energy barriers are not to scale.

dynamics of nanostructures such as islands and steps. How one may extract this information is described in this work. In the following chapter, however, the experimental set-up will be described first.

## **Experimental Set Up**

#### 3.1 The UHV-Chamber

The experiments were performed in an Ultra-High Vacuum (UHV)-chamber (Fig. 3.1.1) with a base pressure of about 5.10<sup>-11</sup>mbar. The low-pressure regime was

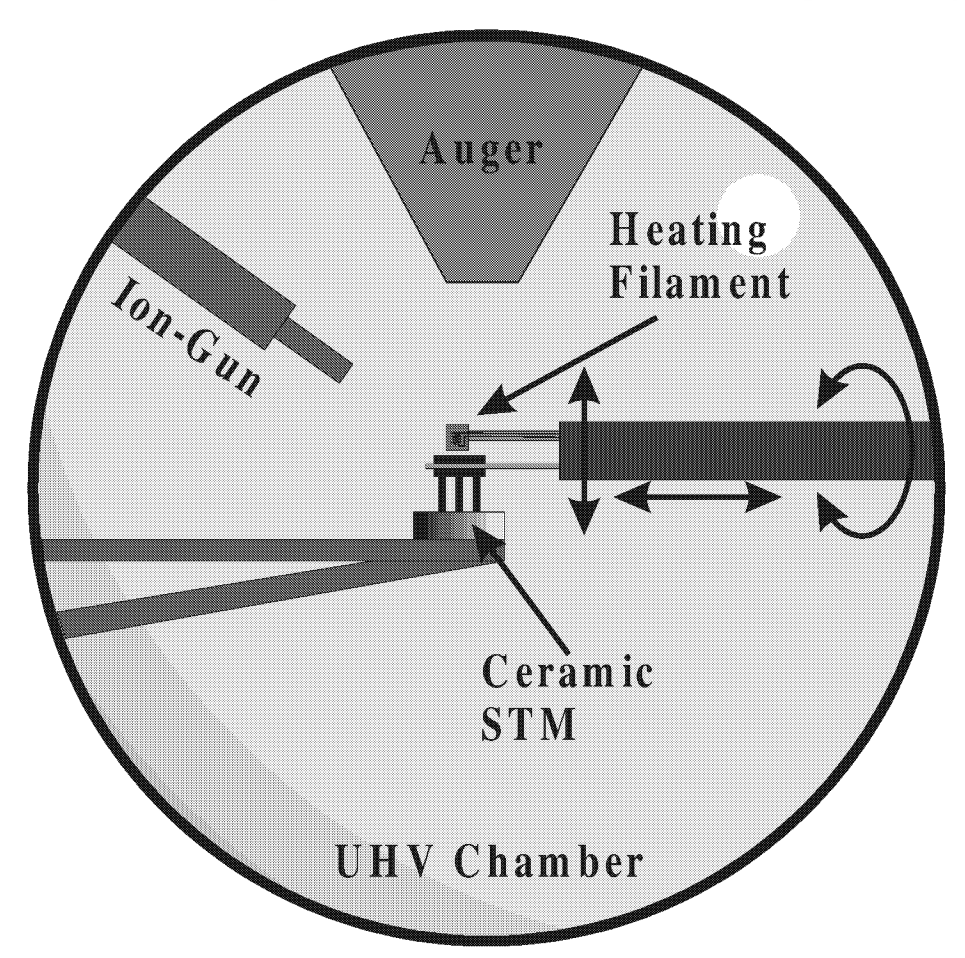


**Figure 3.1.1** The schematics of the UHV-chamber including the ceramic STM. Fixed to the manipulator is the sample. The manipulator is used to bring the sample in position for the ion bombardment and for Auger spectrometry. It is also used to put down the sample onto the STM.

reached using a turbomolecular pump with magnetic bearing supported by a rotary pump as well as by an ion getter pump and a titanium sublimation pump. The first two pumps were disconnected from the UHV chamber during STM measurements to avoid vibrations. In order to isolate the chamber from environmental noise the whole UHV-chamber is positioned on three commercial pneumatic vibration isolators.

The UHV chamber is equipped with a Besocke-type STM [15] using a sample holder by Frohn et al [16]. In contrast to the original design described in [15], the piezo actuators are mounted on a ceramic base plate [17] on which the electrical wiring is evaporated as thin gold coated lines. More details are given in section 3.3. If not located on the STM, the sample fixed in the sample holder is carried by a manipulator, which is operated manually. The manipulator allows moving the sample to the STM and to bring it in position for Auger spectrometry and for ion-bombardment. During the experiment, the sample holder with the sample is mechanically isolated from the manipulator save for the thermocouple connections for which ultra-thin (10 µm) thermocouple wire was used. When the sample is mounted in the manipulator, it can be annealed by electron bombardment using a tungsten filament in a Wehnelt cylinder. During STM recording in an experiment, the filament can be located above the sample such that the sample can be annealed by radiation. Sample temperatures up to 750K can be reached easily. To reach higher temperatures, the sample must be heated by electron bombardment which is typically used, however, merely for sample preparation. The Auger spectrometer with cylindrical mirror analyzer is used to verify the surface cleanliness of the sample. The desired surface morphology with adatom and vacancy islands is produced by ion bombardment using the ion-gun.

### 3.2 Sample preparation

For the STM studies as described in this work, very clean crystal surfaces have to be used. Therefore, the sample preparation and the surface cleaning were important aspects for successful experiments. Caused by the chemical reactivity of platinum, particular care during sample preparation was necessary for the cleaning of the Pt(111) sample.

The cleaning of the Pt(111) surface was performed by a series of repetitive cycles of ion bombardment and sample heating [18]. For ion bombardment, ionized neon atoms were used. They had an energy of 3kV and a flux of about 10μA and the bombardment lasted for 15 minutes. This procedure cleaned the surface in particular from its natural content of carbon, which is the dominant contamination of platinum bulk material. Surface defects were healed and the surface has coarsened by subsequent annealing of the sample to about 1200K. After 15-20 cycles, the surface was free of contaminations as inspected by Auger spectroscopy. The Auger resolution limit is about 1% surface coverage. Since the STM is much more sensitive to residual contamination surface cleaning had to be extended to about 30 cycles. Then, the inspection of the surface by STM showed no residual contamination. Adatom and vacancy islands on Pt(111) were created by sputtering of the surface with neon ions with an energy of 1kV, using an emission current 20mA and an ion flux of about 5μA. By ion bombardment preferentially vacancy islands are produced, however, also adatom islands are frequently observed after surface sputtering.

The sample preparation of the Cu(100) sample did not differ significantly from the above described procedure for Pt(111). For the ion bombardment, a flux of ionized neon atoms of about  $10\mu A$  for 15 minutes was used with an energy of 1.2kV. Due to the lower melting point of copper, for Cu(100) an annealing temperature of 1000 K was used to heal the surface defects after sputtering. The sputtering and annealing cycles were repeated at least 20 times in order to remove the sulfate contamination from the surface. For the last sample annealing, a temperature of 700 K was used to prevent sulfur from the bulk to segregate to the surface. The vacancy islands on the Cu(100)

12 \_\_\_\_ Chapter 3

surface were produced by neon sputtering with an energy of 600 V [19] at the temperature where the measurement was performed.

#### 3.3 The STM

The STM used in this work is a homemade Besocke beetle-type STM [15]. It is mounted on a ceramic base plate with gold wiring described in detail in [17] (Fig. 3.3.1). The sample is mounted in the sample holder which has three ramps used for the coarse approach of the sample to the tip [16]. When the sample is put onto the STM, each of the piezo actuators is positioned at the top of a ramp. Any of the outer piezotubes has three electrodes and by changing the amplitude and the frequency of the voltage applied to the electrodes, the piezo tubes are moved down the ramps of the

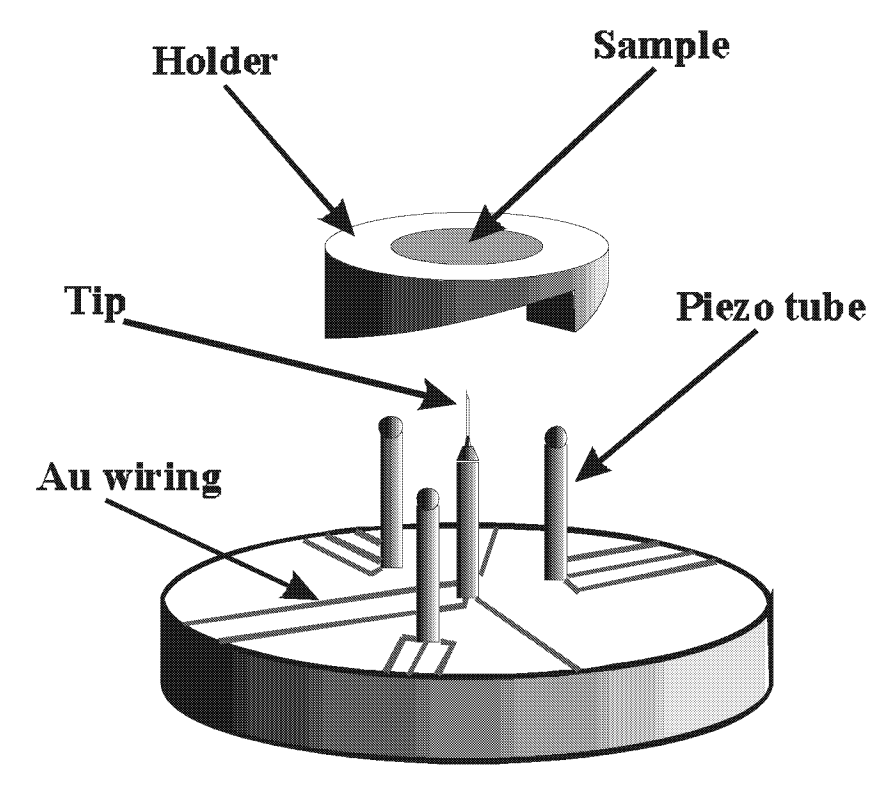


**Figure 3.3.1** Schematic drawing of the STM used in this thesis. The three outer piezo tubes are used to do the coarse approach of the sample to the tunnel tip.

sample holder by means of a "stick-and-slick"-mechanism [16]. As a result, the sample surface approaches the tunneling tip. Finally, the tip is brought into tunneling range by applying a voltage to the central piezo actuator by which the length of the central piezo tube can be changed. The tunneling tip is attached to the central piezo tube and scans the sample surface. The STM is generally run in the constant-current mode and the tunneling current is amplified and transferred to the computer where a digital image of the surface is produced. The tunneling tip is made by electrochemically etching from tungsten wire with a diameter of 0.25 mm. The tunneling current used in the measurements was 2nA. The typical recording time of an STM image was 60-90 s using a  $512 \times 512$  pixel resolution.

For a given sample at a distinct temperature, the STM recording in an experiment could last for 1-3 days, at least for a couple of hours. Therefore, for the studies described in this work a large number of STM-images of the crystal surfaces were recorded (~38000 images total).

#### 3.4 Processing the STM-images

The large number of STM data could be analyzed only by means of an appropriate computer program. The program used in this work guaranteed a fast and accurate way to determine the island boundary and the island area. The developed image recognition program<sup>1</sup> works as follows: for the selected island (Fig. 3.4.1 left) it

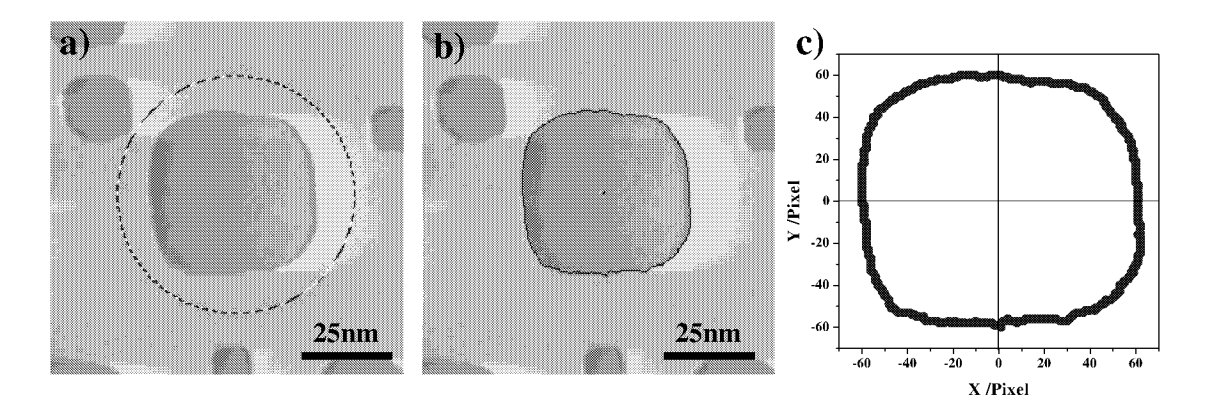


**Figure 3.4.1** Detection of the island perimeter. a) Selected island on the surface. b) The perimeter is found. c) The island perimeter is stored in polar coordinates.

searches for the highest gradient in the pixel color<sup>2</sup>. The edge finding method is simple, although finding a fast and accurate numerical algorithm was kind of a challenge. The idea of this method is illustrated in Fig. 3.4.2. First, a cross section line trough an island is chosen (Fig. 3.4.2 left) and the height profile of this cross section is determined (Fig. 3.4.2 plot A). Since the STM images were recorded with a differentiated height signal, the cross section across the terrace is not a constant value. Small-scale fluctuations in the height values along the cross section are due to noise in the STM image caused by fluctuations in the tunneling current. These fluctuations may influent the accuracy of the

-

<sup>&</sup>lt;sup>1</sup> The initial program was developed by G. Schulze Icking-Konert [17]. In this program, one has to vary manualy several parameters like the slope of the edge, the accuracy and the number of calculated pixels. Each of the parameters may vary for different pictures and have to be adjusted for every next image. This was a time consuming process and provoked the development of a new, more automatic edge detection program.

All of presented STM images in this work have to be interpreted as follows: The dark areas correspond to a deeper layer on the surface, e.g. vacancy islands. The lighter areas correspond to a higher surface layer, e.g. adatom islands. The shadow from left to right is due to the differentiated height values produced by the STM controller.

edge detection. Therefore, for the edge detection an additional step for the signal analysis was introduced: In the derivation of the cross section profile (as shown in Fig. 3.4.2 plot A), the location of the island edge is defined by pronounced sharp peaks (Fig. 3.4.2 plot B) which now can easily be used as exact position of the island perimeter in this cross section. The algorithm of the edge detection program divides the oval selection (Fig. 3.4.1a) in 360 equally spaced angular sectors and determines the cross section lines in each of the sectors starting from the center of the oval. Than it searches for the position of maximum in the absolute value of the derivative, which corresponds

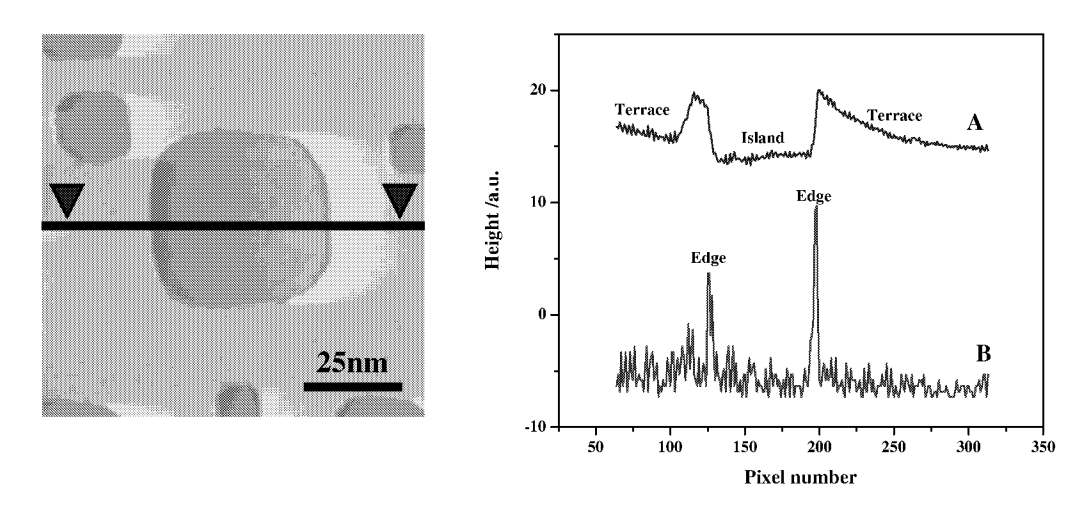


**Figure 3.4.2** One-dimensional cross section of a vacancy island. In the left: The line represents the position of the cross section. In the right: A) Height profile of the cross section; B) Absolute values of the first derivative of the profile. The peaks indicate the positions of the island edges.

to the position of the island edge in this sector. Adding the areas of all the sectors yields the total area of the island which is stored. Once the island boundary is found (Fig. 3.4.1 middle), it is saved as polar coordinates in an ASCII file where the origin is the center of mass of the island. The file is stored for further processing (Fig. 3.4.1 right).

Due to the hysteresis of the piezo actuators, the islands may appear skewed in the STM images. To solve this problem, the measured island shapes were symmetrized using a different program [20].

## Islands in equilibrium

### 4.1 Equilibrium island shape

For not too large temperatures, a crystal surface can be described as a crystallographic flat plane with Miller indices (hkl). Not too large temperatures means here that the temperature T is below the roughening temperature [21] of a distinct facet. At T = 0 K, the ideal surface of a crystal in equilibrium is free of thermal defects. The adatom and vacancy islands are produced only close to the roughening temperature of the surface [21]. The roughening temperature for some surfaces may be close to the bulk melting temperature of the crystal and also, such as for Cu(100), above the melting temperature [21, 22]. Below the roughening temperature, islands on the surface can be generated by deposition or removal of material. This leads to a rough surface far from equilibrium and then, the surface has to be annealed to the temperature where the surface mobility is sufficient to equilibrate the surface structures. The deposited atoms perform a random walk on the surface until they form a stable nucleus. Further atoms are attached to this nucleus and large islands are formed. The shape of the islands depends significantly on the temperature and on the step line tension. At low temperatures and slow edge diffusion, the atoms attach to the island and stick there. Then dendritic growth shapes are formed [23]. When the temperature is high enough and the diffusion is faster, the islands assume their equilibrium shapes, which is determined exclusively by the step line tension and the temperature. The relation between step line tension and equilibrium shape is described by the Wulff construction discussed in the next section.

#### **4.2 Wulff Construction**

For three-dimensional crystals, the surface free energy per unit area  $\gamma(\vec{m},T)$  is a function of temperature T and orientation  $\vec{m}$ . For two-dimensional islands, the analogous quantity to  $\gamma(\vec{m},T)$  is the step free energy  $\beta(\vec{m},T)$ . The orientation dependence of the surface free energy is called anisotropy of the surface free energy. The equilibrium crystal shape is defined only in the limit  $V \to \infty$  (for three dimensional crystals, where V is the volume of the crystal), respectively,  $A \to \infty$  (for two-dimensional islands, where A is the area of the island). That is, for a given temperature, crystals as well as islands have distinct equilibrium shapes as long as their sizes are large enough. In other words, the number of atoms in the crystals/islands is large enough that the macroscopic limit is valid. When the lengths are rescaled by  $V^{1/3}$ , the atomic-scale fuzziness disappears and the crystal shape is scale invariant.

The equilibrium shape of a large crystal is described by the radius vector  $\vec{R}(\vec{n})$  where  $\vec{n}$  is the unit vector from the center of the crystal to the crystal shape (Fig. 4.2.1). Now by rescaling  $\vec{R}(\vec{n})$  for a given temperature and taking the limit as the volume tends to infinity, the equilibrium shape of the crystal is defined as [23]

$$\mathbf{r}(\vec{\mathbf{n}}) = \lim_{\mathbf{V} \to \infty} \left( \frac{\mathbf{R}(\vec{\mathbf{n}})}{\alpha \mathbf{V}^{1/3}} \right), \tag{4.2.1}$$

where  $\alpha$  may be chosen arbitrarily and  $\vec{n}$  is the unit vector from the center of the crystal.

There exists a famous geometrical representation of equation (4.2.1) [24]. If the crystal occupies the space  $\Omega$  and the interface of the crystal is given by  $\partial\Omega$ , the total free energy is [23]

$$F(T) = \int_{\partial\Omega} dS \gamma(\vec{m}, T) = \int_{\partial\Omega} d\vec{S} \cdot \vec{m} \gamma(\vec{m}, T), \qquad (4.2.2)$$

Wulff construction 19

where  $d\vec{S}=dS\cdot\vec{k}$  is the surface unit,  $\vec{k}$  is a unit vector perpendicular to the surface and  $\vec{m}$  is the unit vector from the center of the crystal (Fig. 4.2.1) to the plot of total free energy  $\gamma$  in polar coordinates (here the origin is identical to the center of the crystal). The volume of the crystal is (where  $d\vec{r}=\left(dx,dy,dz\right)$  and  $\vec{\nabla}=\left(\frac{\partial}{\partial x},\frac{\partial}{\partial y},\frac{\partial}{\partial z}\right)$ ):

$$V(\Omega) = \int_{\Omega} d\vec{r} = \frac{1}{3} \int_{\Omega} \vec{\nabla} \cdot \vec{r} d\vec{r} = \frac{1}{3} \int_{\partial\Omega} d\vec{S} \cdot \vec{r}.$$
 (4.2.3)

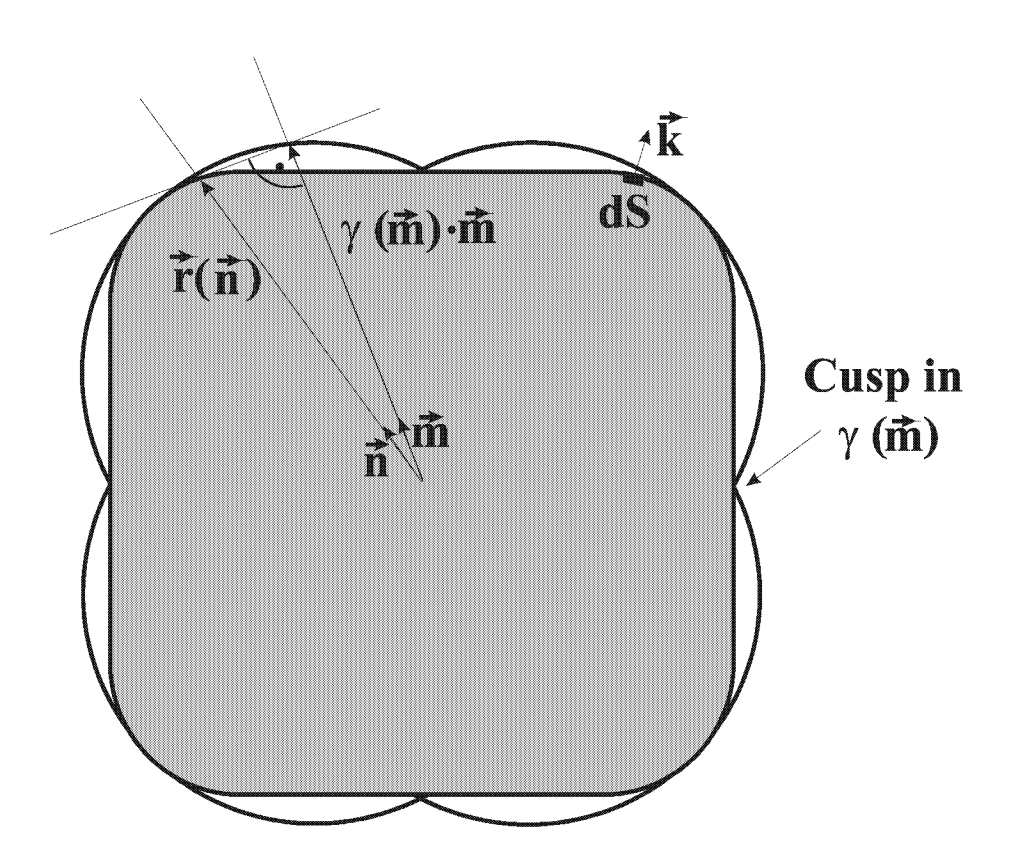


**Figure 4.2.1** *Wulff construction. See text for explanation.* 

If  $\partial\Omega$  changes its shape, F(T) changes and the equilibrium shape of the crystal  $r(\vec{n})$  is the shape which minimizes equation (4.2.2). This minimization problem has an unique solution [25]:

$$\mathbf{r}(\vec{\mathbf{n}}) = \min_{\vec{\mathbf{m}}} \left[ \frac{\gamma(\vec{\mathbf{m}})}{\vec{\mathbf{m}} \cdot \vec{\mathbf{n}}} \right]. \tag{4.2.4}$$

Equation (4.2.4) has a graphical representation known as the Wulff construction [24] (fig. 4.2.1). In the Wulff construction,  $\gamma(\vec{m})$  is drawn as a polar plot (the so called "Wulff plot" or " $\gamma$ -plot") and the equilibrium crystal shape is the interior envelope of the family of perpendicular planes passing through the ends of the radius vectors  $\vec{m}\gamma$ . When there is a cusp in the Wulff-plot, as for instance visible in Fig. 4.2.1, the crystal shape contains crystallographic facets. Vanishing of the facet (and hence, the cusp in the  $\gamma$ -plot) at a given temperature indicates the surface roughening temperature for the given orientation.

For two-dimensional islands, equation (4.2.4) has an analogous form [25]:

$$\mathbf{r}(\vec{\mathbf{n}}) = \min_{\vec{\mathbf{m}}} \left[ \frac{\beta(\vec{\mathbf{m}})}{\vec{\mathbf{m}} \cdot \vec{\mathbf{n}}} \right]. \tag{4.2.5}$$

For a temperature T>0K, steps are always rough even when they are oriented on the average along an atomically dense packed direction [9]. This means that the island perimeter does not reveal real facets. The island segments which appear straight are always slightly curved and there are no cusps in the Wulff-plot.

In order to determine the interface free energy  $\gamma$  from a given equilibrium shape one may use the so-called inverse Wulff construction [23]. From equation (4.2.4) one finds [25]

$$\gamma(\vec{\mathbf{m}})^{-1} = \min_{\vec{\mathbf{m}}} \left[ \frac{|\mathbf{r}(\vec{\mathbf{n}})|^{-1}}{\vec{\mathbf{m}} \cdot \vec{\mathbf{n}}} \right]. \tag{4.2.6}$$

Wulff construction 21

In Fig. 4.2.2, the graphic representation of equation (4.2.6) in two dimensions is shown. In two dimensions, as is the case for islands on the surface, equation (4.2.6) can be inverted easily. In this work, the two dimensional inverse Wulff construction is used to determine the step free energy  $\beta$ : Two-dimensional islands have been displayed with the STM and the equilibrium shape was determined. Using the inverse Wulff construction, the relative step free energies were measured (see section 4.4): First, the

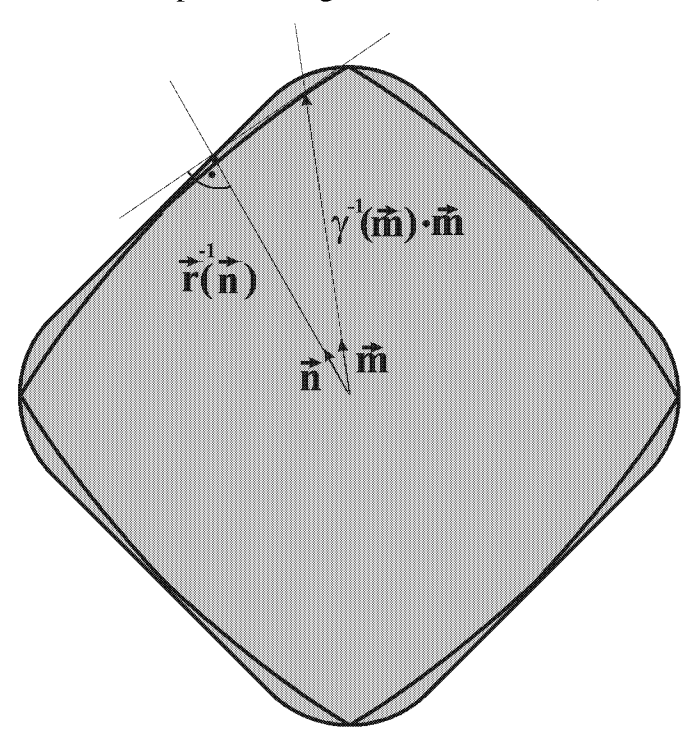


**Figure 4.2.2** *Inverse Wulff construction, used to determine the interface free energy from a given equilibrium shape.* 

perimeter of the equilibrium island shape was divided into 360 equally spaced sectors. In each sector, a line was drawn from the center of the equilibrium shape to the sector segment of the island perimeter and elongated beyond it. Then, a perpendicular line to the radial sector line trough its end point was constructed. The radial sector line was chosen long enough, the perpendicular line through its end point neither touches the island equilibrium shape nor intersects it. Now, the perpendicular line is shifted along the radial sector line towards the center of the island shape. Eventually, the perpendicular line touches the island perimeter as a tangential line. Then, the shifting is

stopped and the section between the island shape center and the crossing point of the radial sector line and the perpendicular line determines the step free energy for this sector orientation. The procedure is repeated with all sectors until the full angle dependence of the step free energy is obtained.

Fig. 4.2.3 shows the equilibrium shapes of islands on fcc (100) and (111) surfaces together with the Wulff-plots of the step free energies. The local maxima and minima of  $\beta$  are indicated by arrows. For the fcc (100) island, the ratio of the minimum and maximum energy  $\beta_{0^{\circ}}/\beta_{45^{\circ}}$  can by directly obtained by the ratio of the respective island radii  $r_{0^{\circ}}/r_{45^{\circ}}$ . The same is true for the trigonal islands when the island has a hexagonal shape. Here, however, the maximum value of  $\beta$  is not assumed in the corner region, i.e.  $\theta = 30^{\circ}$ , but for  $\theta = 60^{\circ}$ . If  $r_{0^{\circ}} \neq r_{60}$ , i.e. if the islands have the shape of truncated triangles (as in the case for Pt(111)),  $\beta_{0^{\circ}}/\beta_{30^{\circ}} \neq r_{0^{\circ}}/r_{30}$ . However, the ratio

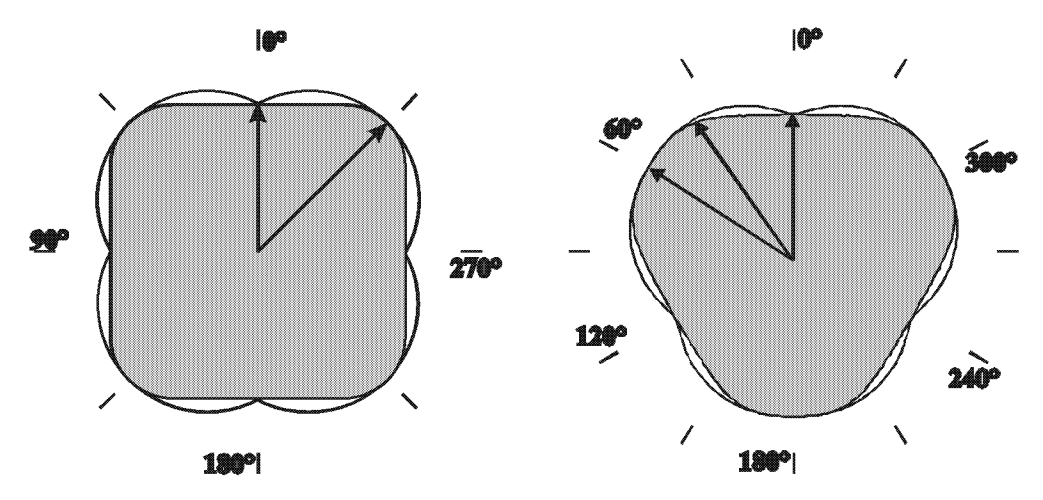


**Figure 4.2.3** Extrema in the step free energy of islands on fcc(100) (left) and fcc(111) (right) surfaces.

between the free energies of A- and B-steps,  $\beta_{0^{\circ}}/\beta_{60^{\circ}}$ , is still equal to the ratio of the respective radii, i.e.  $\beta_{0^{\circ}}/\beta_{60^{\circ}} = r_{0^{\circ}}/r_{60}$ .

### 4.3 Island shape fluctuations

Islands on the surface at a given temperature assume the equilibrium shape only on a long-time average. Dynamic processes such as attachment/detachment of atoms at the island perimeter or atomic diffusion along the island edge cause the island shape to fluctuate around the equilibrium shape. The relation between the island shape fluctuations and the mean step free energy has first been described by Khare and Einstein [8, 26] and applied experimentally by Schlößer et al. [5]. A more detailed theoretical discussion has been reported by Steimer et al. [6, 7]. In the following, a brief description of the theory of island edge fluctuations is explored.

The perimeter of the island at time t is described by the time and angle dependent radius-vector  $\mathbf{R}(\theta,t)$  (Fig. 4.3.1). The perimeter of the equilibrium shape  $\mathbf{r}(\theta)$  is a normalized time average of  $\mathbf{R}(\theta,t)$ . The normalization ensures that the areas enclosed by  $\mathbf{R}(t,\theta)$  and  $\mathbf{r}(\theta)$  are equal. Here we choose  $\theta=0^{\circ}$  to be the angle, where the equilibrium shape has the minimum curvature. The relative variation of the perimeter is defined in polar coordinates as

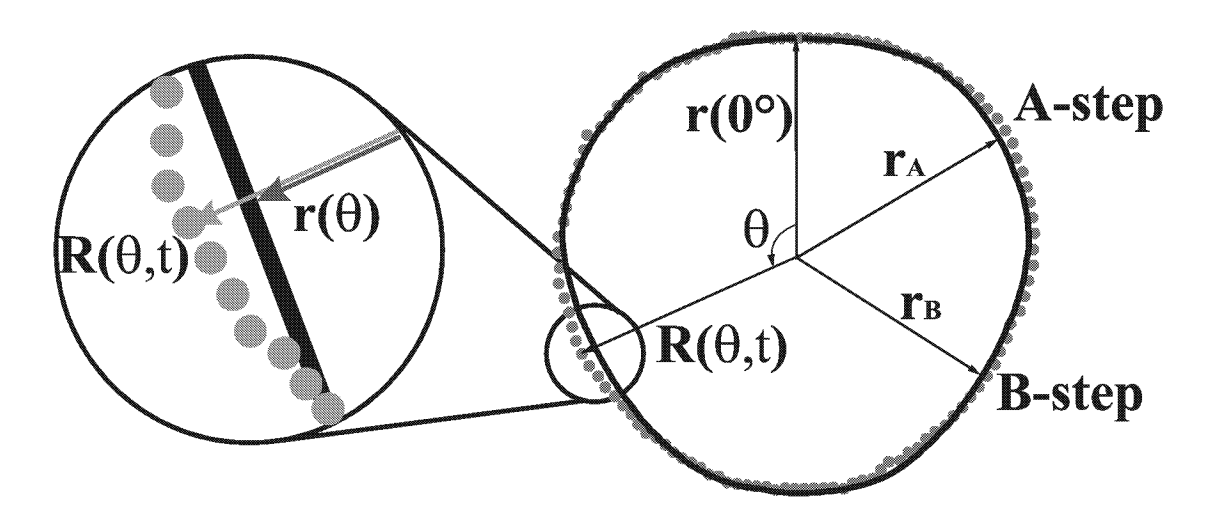


**Figure 4.3.1** Equilibrium shape (solid line) and real island perimeter (doted line). Both are normalized to have equal areas. See text for explanation.

24 \_\_\_\_\_ Chapter 4

$$g(\theta,t) = \frac{R(\theta,t) - r(\theta)}{r(\theta)},$$
(4.3.1)

and it can be expanded in a Fourier series

$$g(\theta, t) = \sum_{n} g_{n}(t) \exp(in\theta). \tag{4.3.2}$$

Since  $g(\theta,t)$  is real, the Fourier coefficients fulfill  $g_n(t)=g_{-n}*(t)$ . The time average of  $g(\theta,t)$  is defined as the fluctuation function G(t)

$$G(t) = \frac{r^2}{2\pi} \int_0^{2\pi} g^2(\theta, t) d\theta, \qquad (4.3.3)$$

where the mean radius r is given by

$$\mathbf{r} = \frac{1}{2\pi} \int_{0}^{2\pi} \mathbf{r}(\boldsymbol{\theta}) d\boldsymbol{\theta}. \tag{4.3.4}$$

By inserting (4.3.2) in (4.3.3) the fluctuation function can be expressed in a Fourier series:

$$G(t) = r^2 \sum_{n} |g_n(t)|^2$$
 (4.3.5)

The total free energy F(t) of the island perimeter is the integral of the step free energy along the island perimeter:

$$F(t) = \oint_{r(\theta,t)} \beta ds = \int_{0}^{2\pi} \beta(\theta) \sqrt{R^{2}(\theta,t) + \left(\frac{\partial R(\theta,t)}{\partial \theta}\right)^{2}} d\theta.$$
 (4.3.6)

Due to the fluctuations, the time average of the total free energy F(t) is larger than  $F_0$ . Hence, the island equilibrium shape is given by the minimum in the total free energy min $[F(t)]\equiv F_0$ . By inserting  $R(\theta,t)=r(\theta)(g(\theta,t)+1)$  from (4.3.1) in (4.3.6), the difference between the time average of F(t) and  $F_0$  can be expressed by the time averaged Fourier coefficients of the fluctuation function (see [6] for a detailed description):

$$\langle \Delta F \rangle_{t} = \langle F - F_{0} \rangle_{t} = \langle F \rangle_{t} - F_{0} = \pi \overline{\beta} r \sum_{|n|>1} (n^{2} - \sigma) \langle |g_{n}(t)|^{2} \rangle_{t}. \tag{4.3.7}$$

Here,  $F_0 = \oint_r \beta dS$  is a free energy contribution from the equilibrium shape. From equation (4.3.7), one finds that the contribution of the fluctuations to the free energy is proportional to the mean step free energy  $\overline{\beta}$  defined as

$$\overline{\beta} = \frac{1}{2\pi} \int_{0}^{2\pi} B(\theta) d\theta, \qquad (4.3.8)$$

where

$$B(\theta) = \frac{\beta(\theta)}{r} \frac{r^{4}(\theta)}{\left[r^{2}(\theta) + \left(\frac{\partial r(\theta)}{\partial \theta}\right)^{2}\right]^{\frac{3}{2}}}.$$
(4.3.9)

The parameter  $\sigma$  in equation (4.3.7) depends on the equilibrium shape and is given by [6]

$$\sigma = \frac{1}{2\pi} \int_{0}^{2\pi} A(\theta) d\theta, \qquad (4.3.10)$$

with

$$A(\theta) = \frac{\beta(\theta) \sqrt{r^2(\theta) + \left(\frac{\partial r(\theta)}{\partial \theta}\right)^2}}{\overline{\beta} r}.$$
 (4.3.11)

For islands with a circular shape  $(\partial r(\theta)/\partial \theta = 0)$ ,  $\sigma$  has a minimum value equal to one. Any deviation from the circular shape increases  $\sigma$ . In the classical continuum model, each of the modes in equation (4.3.7) contributes  $k_BT/2$  to the free energy and then [26]

$$\left\langle \left| g_{n}(t) \right|^{2} \right\rangle_{t} = \frac{k_{B}T}{2\pi \overline{\beta} r(n^{2} - \sigma)}$$
 (4.3.12)

and

$$\left\langle G(t)\right\rangle_{t} = \frac{k_{B}rT}{2\pi\overline{\beta}} \sum_{|\mathbf{n}|>1} \frac{1}{\mathbf{n}^{2} - \sigma}.$$
 (4.3.13)

Calculating the sum in equation (4.3.13) one finds [6]:

$$\sum_{|n|>1} \frac{1}{n^2 - \sigma} = \frac{-\Psi(2 - \sqrt{\sigma}) + \Psi(2 + \sqrt{\sigma})}{\sqrt{\sigma}},$$
(4.3.14)

where  $\Psi(x)$  is the derivative of the logarithm of the gamma-function:

$$\Psi(x) = \frac{\partial (\ln \Gamma(x))}{\partial x}.$$
(4.3.15)

For the circular island shape ( $\sigma$ =1), the sum in equation (4.3.14) has a value of 3/2. This sum depends merely weakly on  $\sigma$ , and hence, on the island shape. For real island shapes, the deviation of  $\sigma$  from 1 is small and the relative error introduced when the step free energy is determined under the assumption of circular islands can be neglected. For example, in the case of quadratic islands at room temperature the relative error is less than 5% [7]. In particular for islands at higher temperatures, the island shape is closer to a circular equilibrium shape, and then the sum in equation (4.3.14) can be assumed to be 3/2. In the following, the sum in equation (4.3.14) is therefore set to a value 3/2. Then, the time averaged fluctuations function becomes [5]

$$\left\langle G(t)\right\rangle_{t} = \frac{3k_{B}rT}{4\pi\overline{\beta}}.$$
 (4.3.16)

As can be seen from equation (4.3.16), the fluctuation function is determined by the mean step free energy  $\overline{\beta}$ , the temperature T and the mean radius of the island. By inserting the definition of the fluctuation function (equation (4.3.3) using (4.3.1)) into (4.3.16) and dividing by  $r^2$  one finds for the normalized fluctuation function:

$$\frac{\left\langle G(t)\right\rangle_{t}}{r^{2}} = \left\langle \left\langle \left(\frac{R(\theta, t) - r(\theta)}{r(\theta)}\right)^{2}\right\rangle_{\theta}\right\rangle_{t} =$$

$$= \left\langle \frac{1}{2\pi} \int_{0}^{2\pi} \left(\frac{R(\theta, t) - r(\theta)}{r(\theta)}\right)^{2} d\theta\right\rangle_{t} = \frac{3k_{B}T}{4\pi\overline{\beta}r}$$
(4.3.17)

Equation (4.3.17) describes the dependence of the normalized mean square deviation of a single island shape on the mean island size and the temperature.

In experimental data, an additional contribution to the fluctuation function  $\left\langle G\right\rangle_t$  must be considered: The experimental error  $\left\langle G_{0\text{exp}}\right\rangle_t$ , which is introduced by the digital recognition of the island perimeter in an STM image. For any of the detected

points in the perimeter there is a term  $\Delta R(\theta,t)$ , which is half the size of a pixel. Obviously, the magnitude of  $\Delta R(\theta,t)$  depends on the scan width, if the number of pixels per image is kept constant. Adding  $\left\langle G_{\theta exp} \right\rangle_t$  to the fluctuation function in equation (4.3.17) leads to

$$\left\langle G_{\exp} \right\rangle_{t} = \frac{r^{2}}{2\pi} \left\langle \int_{0}^{2\pi} \left( \frac{R(\theta, t) + \Delta R(\theta, t) - r(\theta)}{r(\theta)} \right)^{2} d\theta \right\rangle_{t} =$$

$$= \left\langle G \right\rangle_{t} + \left\langle \left\langle (\Delta r(\theta, t))^{2} \right\rangle_{\theta} \right\rangle_{t} = \left\langle G \right\rangle_{t} + \left\langle G_{0\exp} \right\rangle_{t}$$

$$(4.3.18)$$

As long as  $\Delta r(\theta,t)$  is statistically independent of  $r(\theta,t)$  and  $R(\theta)$ , the averaging can be performed separately.  $\left\langle G_{0exp} \right\rangle_t$  is a positive value, which has to be subtracted from the experimental data.

As will be shown in the next section,  $\overline{\beta}$  can be used to obtain absolute step free energies, if the relative step free energies have been determined using the inverse Wulff-construction.

# 4.4 Determination of the step free energies on the Pt(111) surface

The measurements were performed in a temperature regime between 573K and 713K. The islands on Pt(111) assume a shape of truncated triangles (Fig. 4.4.1) because the step energies of A- and B-steps deviate by about 13% [18].

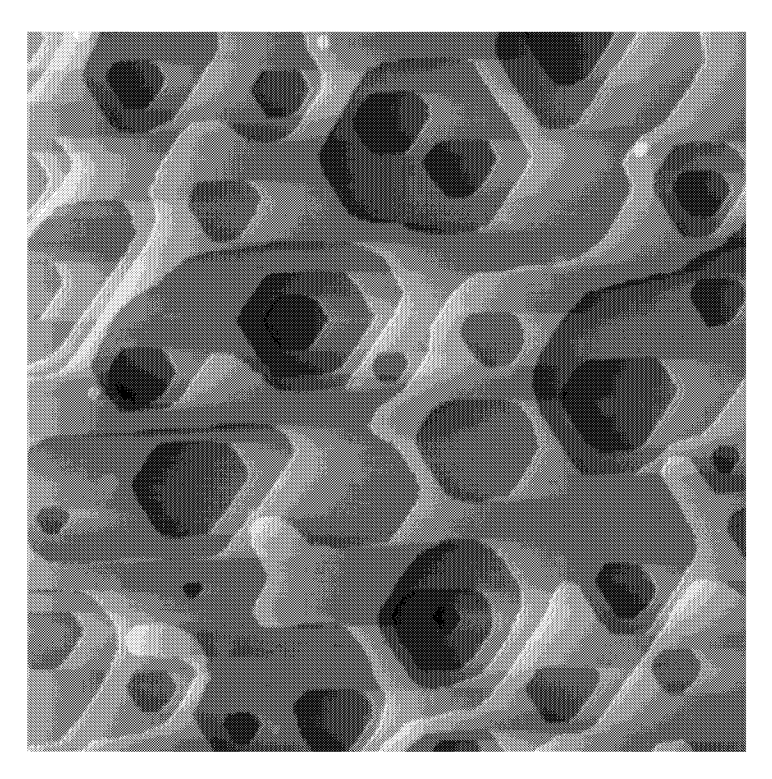


**Figure 4.4.1** STM-image of the Pt(111) surface at 633K with vacancy islands. The vacancy islands have a shape of truncated triangles. The scan width is 194.4 nm.

To determine the equilibrium shape, a large number of individual island shapes were averaged for all temperatures. In Table 4.4.1, the number of island shapes for a given temperature used to determine the equilibrium shape is shown.

**Table 4.4.1** The number of islands used to determine the equilibrium shape for a given temperature.

T(K)	533	573	593	613	633	653	673	713
Number of islands	573	479	509	320	806	661	946	278

The equilibrium shape depends on the temperature (Fig.4.4.2) and becomes rounder with higher temperatures. The equilibrium shapes shown in Fig. 4.4.2 are not to scale, the way they are plotted is merely used to demonstrate the shape change with temperature. The ratio  $r_A/r_B$ , which is equal to the ratio  $\beta_A/\beta_B$ , changes also with temperature. In Fig. 4.4.3, the temperature dependence of  $r_A/r_B$  between 533K and 713K is shown. With increasing temperature, the ratio  $r_A/r_B$  slightly decreases, e.g. the difference in the step free energies of both step types on Pt(111) becomes smaller.

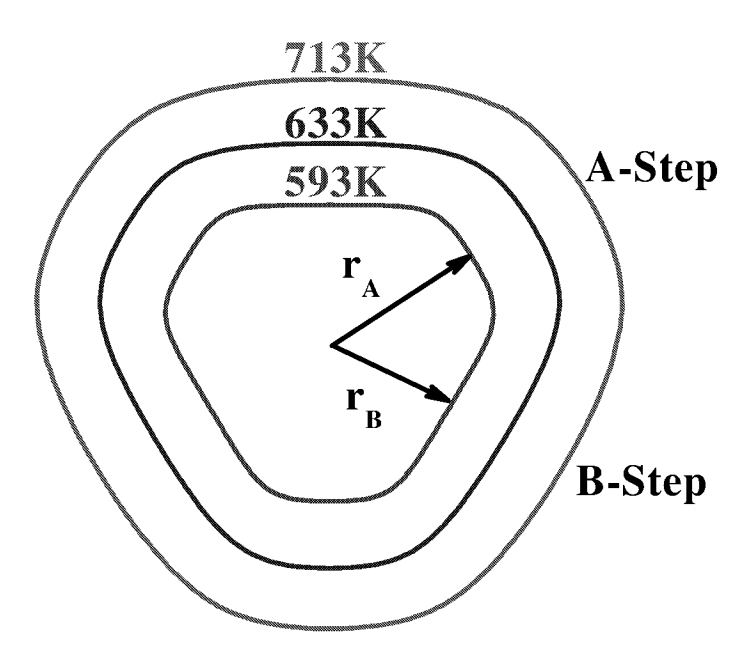


**Figure 4.4.2** *Measured equilibrium shapes for Pt(111) at three distinct temperatures. With increasing temperature the shape becomes rounder.* 

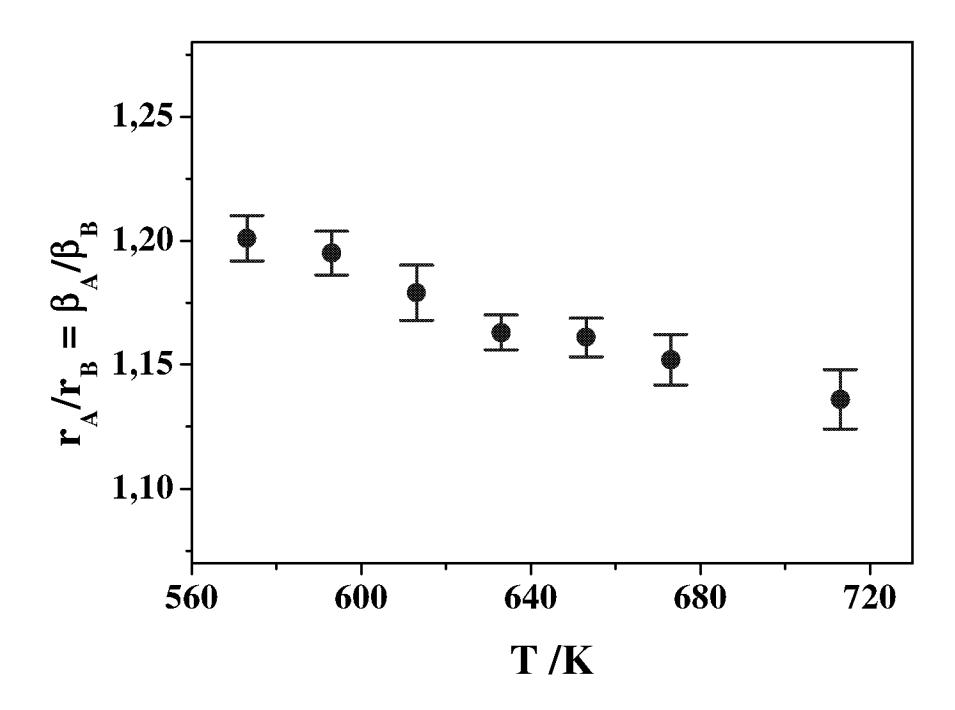


**Figure 4.4.3** The ratio of the radii for A- and B-steps in equilibrium shapes on Pt(111) vs. temperature. The ratio is equal to the ratio of the step free energies for A- and B-steps.

The relative free energies of the A- and B-steps on Pt(111) were determined using an inverse Wulff construction of the measured equilibrium shapes. The inverse Wulff construction was made such was described in section 4.2. Figure 4.4.4 shows the anisotropy of the step free energy  $\beta(\theta)$  along the island perimeter for T=593 K (squares), T=633 K (triangles) and T=713 K (circles). Due to the trigonal symmetry of the islands, the Wulff plot  $\beta(\theta)$  is periodic in  $2/3\pi$ . Therefore, the Wulff plot in Fig. 4.4.4 is shown exclusively for angles between  $\theta=0^\circ$  and  $\theta=120^\circ$ . The values in the Wulff-plot are normalized with respect to the step energy at  $\theta=0^\circ$  corresponding to the energy of the B-step. The value of  $\beta$  at  $\theta=60^\circ$  corresponds to the step free energy of the A-step. Hence, the ratio  $\beta(\theta=60^\circ)/\beta(\theta=0^\circ)$  represents the ratio  $\beta_A/\beta_B$ . For two dimensional islands and in the case of nearest-neighbor interactions, islands on crystal surfaces never have straight steps at temperatures T>0K. This is due to the fact that the one-dimensional island perimeter is above its roughening transition [21] for temperatures higher than T=0 K. That is, island steps never reveal one-dimensional

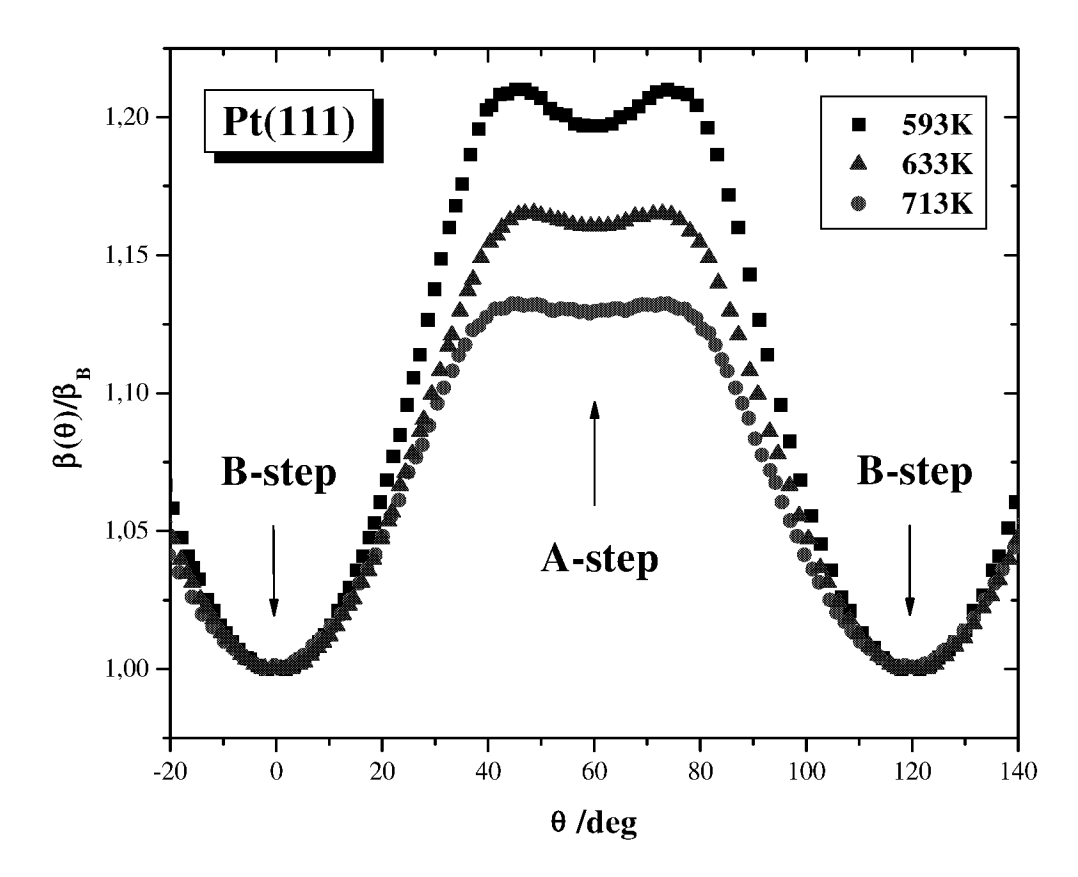


**Figure 4.4.4** Wulff-plot  $\beta(\theta)$  for Pt(111) for three different temperatures T=593 K (squares), T=633 K (triangles), T=713 K (circles). The values are normalized to the free energy of B-Step.

facets. Therefore, the Wulff-plots of islands such as shown in Fig. 4.4.4 never have cusps.

The Wulff plot as shown in Fig. 4.4.4 for Pt(111) can exclusively yield relative step free energies, i.e.  $\beta(\theta)/\beta_B$ . In order to determine the absolute values for  $\beta_A$  and  $\beta_B$  one has to make use of the result for the mean step free energy  $\overline{\beta}$  as obtained from the island shape fluctuations: For the determination of the island edge fluctuations, the island shapes measured at a distinct temperature were divided into subgroups of islands of about the same size. Within the subgroup, variations of the island radius of  $\pm 10\%$  were allowed. For each subgroup, the fluctuation function  $\left\langle G(t) \right\rangle_t$  (equation (4.3.16)) was calculated separately. Fig. 4.4.5 shows the time averaged fluctuation function  $\left\langle G(t) \right\rangle_t$  (equation (4.3.16)) versus the product of the temperature and the mean island radius. The experimental values are plotted as full symbols. As discussed before, one

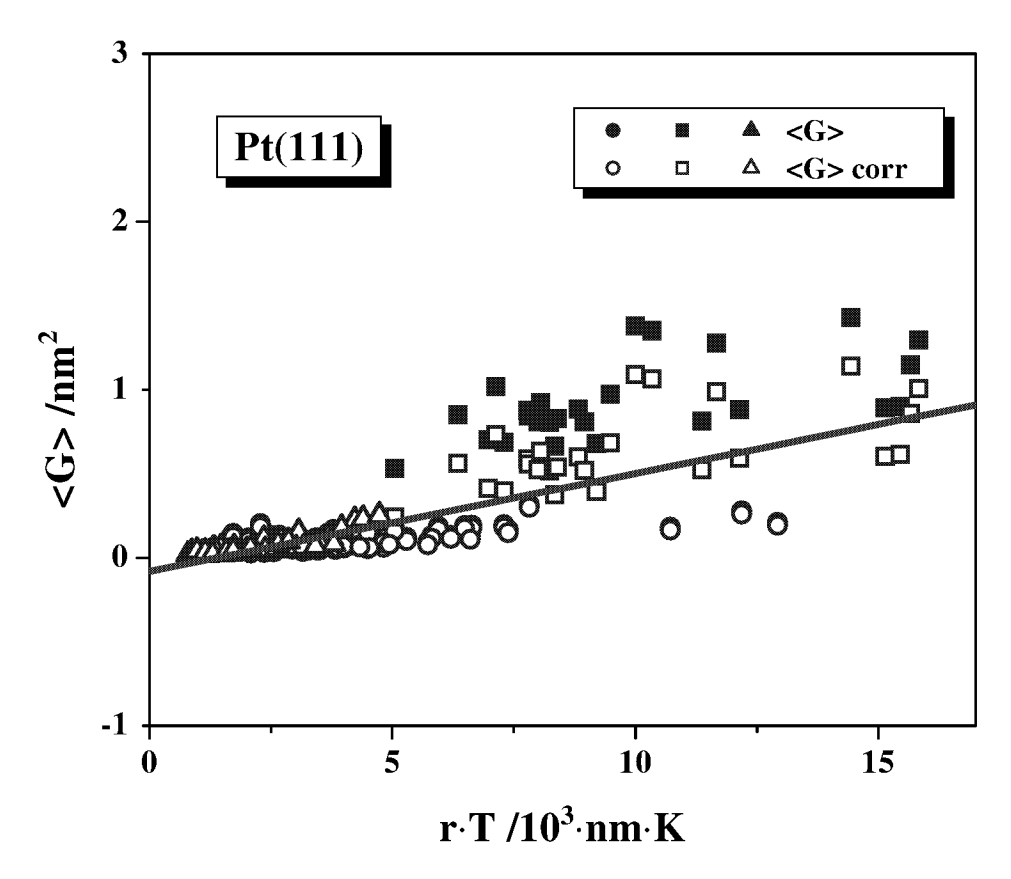


**Figure 4.4.5** The time averaged fluctuation function vs. the product of the mean island radius and temperature. The values, corrected by the equation (4.3.18) are plotted with open symbols. The correction is different for the different scan widths of the measured STM-images. The values measured at scan width 388.8nm, 194.4nm and 97.2nm are plotted with squares, circles and triangles respectively. The linear fit is inverse proportional to the mean step free energy.

may account for the pixel error in the determination of the island perimeter by using equation (4.3.18) for  $\langle G(t) \rangle_t$  instead of equation (4.3.16). The open symbols in Fig. 4.4.5 are the experimental data for  $\langle G(t) \rangle_t$  corrected for the pixel error by using equation (4.3.18). The values were measured at scan widths 388.8 nm (squares), 194.4 nm (circles) and 97.2 nm (triangles). According to equation (4.3.16), the slope of the linear fit to the experimental data is inverse proportional to the mean step free energy per atom unit. From Fig. 4.4.5, one finds a slope of  $5.8 \times 10^{-5} \pm 2.7 \times 10^{-6}$  nm/K. Hence,  $\overline{\beta}$  for Pt(111) is determined to:

$$a_{\parallel}\overline{\beta} = \frac{3k_{B}}{4\pi} \frac{1}{\langle G(t) \rangle_{t} / rT} =$$

$$= \frac{3k_{B}}{4\pi} \frac{1}{(5.8 \times 10^{-5} \pm 2.7 \times 10^{-6} [\text{nm/K}])} = 353 \pm 17 \text{ meV}$$
(4.4.1)

where  $a_{\parallel}$  is the atomic unit parallel to the step.

To obtain the absolute values of the step free energies for A- and B-steps from the mean step free energy  $\overline{\beta}$ , one now uses the known anisotropy of the step free energy  $\beta(\theta)$ . By inserting equation (4.3.9) into equation (4.3.8) and dividing both sides of the equation by  $\beta(\theta=0^\circ)$ , as well as multiplying the right hand side of the equation by  $r^4(\theta=0^\circ)/r^4(\theta=0^\circ)$ , one obtains

$$\frac{\overline{\beta}}{\beta(\theta=0^{\circ})} = \frac{1}{2\pi} \int_{0}^{2\pi} \frac{\beta(\theta)}{\beta(\theta=0^{\circ})} \frac{r_{n}^{4}(\theta)}{\left[r_{n}^{2}(\theta) + \left(\frac{\partial r_{n}(\theta)}{\partial \theta}\right)^{2}\right]^{\frac{3}{2}}} d\theta.$$
(4.4.2)

Here,  $r_n=r/r(\theta=0^\circ)$  is the normalized mean radius and  $r_n(\theta)=r(\theta)/r(\theta=0^\circ)$  is the normalized radius of the equilibrium shape. Using equation (4.4.2), the mean step free energy normalized to the value of step free energy at  $\theta=0^\circ$  can be calculated by means of the values determined from the equilibrium shape and the inverse Wulff construction. In Fig. 4.4.6, the angle dependence of the radius of the equilibrium shape, normalized to the radius at  $\theta=0^\circ$  and the step free energy normalized to the value at  $\theta=0^\circ$  are given for a temperature of T=633K, which corresponds to the average temperature of the studied range between 593 K and 713 K. Solving equation (4.4.2) by using the values shown in Fig. 4.4.6, one finds the normalized value of the mean step free energy per atom unit:

$$\frac{a_{\parallel}\overline{\beta}}{a_{\parallel}\beta(0)} = \frac{a_{\parallel}\overline{\beta}}{a_{\parallel}\beta_{\rm B}} = 1.036. \tag{4.4.3}$$

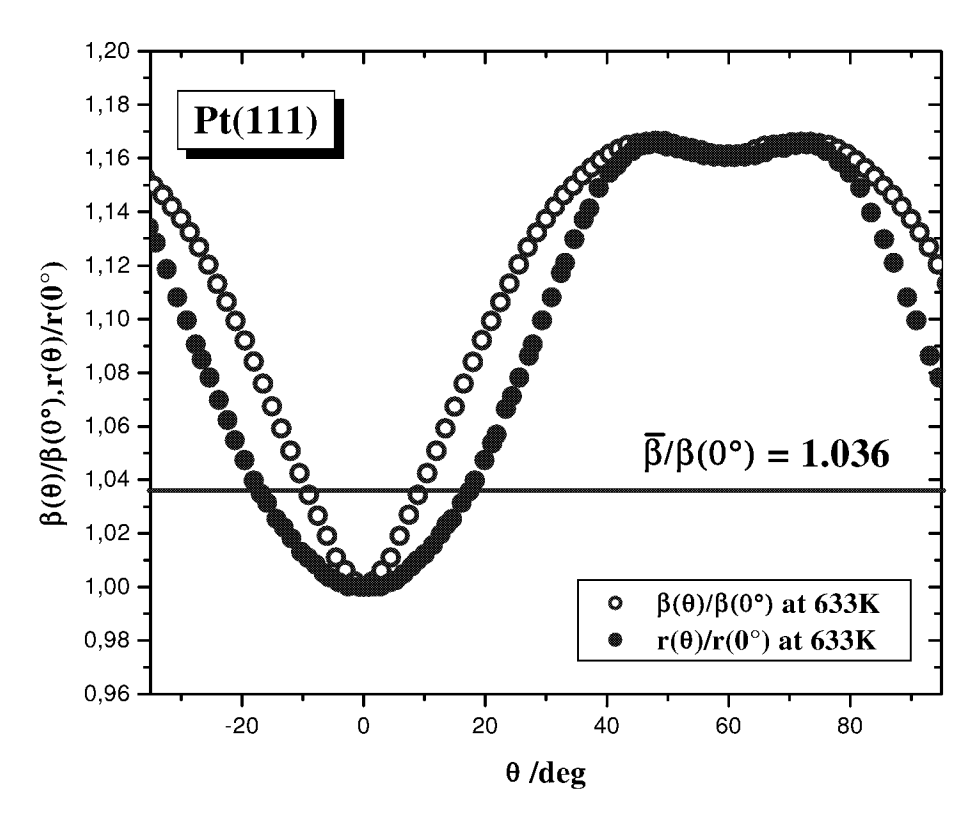


**Figure 4.4.6** Plot of  $\beta(\theta)/\beta(0^{\circ})$  and  $r(\theta)/r(0^{\circ})$  at 633 K to determine the absolute step free energies  $\beta_A$  and  $\beta_B$ . See text for discussion.

Since  $a_{\parallel}\overline{\beta}$  is known, the absolute value for the free energy per atom unit of the B-step is obtained to

$$a_{\parallel}\beta_{B} = 340 \pm 17 \,\text{meV}$$
. (4.4.4)

After finding the step free energy for B-step and because of

$$\frac{a_{\parallel}\beta_{A}}{a_{\parallel}\beta_{B}} = \frac{r_{A}}{r_{B}} = 1.16 \tag{4.4.5}$$

at 633 K (Fig. 4.4.6) one obtains the step free energy per atom unit of the A-step to be

$$a_{\parallel}\beta_{A} = 395 \pm 17 \,\text{meV}$$
. (4.4.6)

The experimentally obtained values for the step free energies of A- and B-steps  $\beta_A = 395 \pm 17 \text{ meV} \text{ and } \beta_B = 340 \pm 17 \text{ meV} \text{ per atom may be compared with results by}$  Feibelmann [27-30], Boisvert et al [31], Nelson et al [32] and Michely et al [18]. Table 4.4.1 summarizes the experimental and theoretical data for  $\overline{\beta}$ ,  $\beta_A$  and  $\beta_B$ .

**Table 4.4.1** Experimental and theoretical data for the step free energies on Pt(111) as obtained in this work and as reported in cited publications.

	a <sub>  </sub> β̄ (meV)	a <sub>  </sub> β <sub>A</sub> (meV)	$a_{\parallel}\beta_{B}$ (meV)	$\begin{bmatrix} \mathbf{a}_{\parallel} \boldsymbol{\beta}_{\mathrm{A}} + \mathbf{a}_{\parallel} \boldsymbol{\beta}_{\mathrm{B}} \\ (\text{meV}) \end{bmatrix}$	$a_{\parallel}\beta_{A}/a_{\parallel}\beta_{B}$
Experiment (This work) (573K <t<713k)< td=""><td>353 ± 17</td><td>395 ± 17</td><td>340 ± 17</td><td>735 ± 17</td><td>1.16 ± 0.05</td></t<713k)<>	353 ± 17	395 ± 17	340 ± 17	735 ± 17	1.16 ± 0.05
Experiment [18] (700K <t<925k)< td=""><td></td><td></td><td></td><td></td><td>1.15±0.03</td></t<925k)<>					1.15±0.03
LDA [30]		400	350	750	1.14
LDA [31]		430	380	810	1.14
EAM [32]		344	341	685	1.01

Michely et al [18] analyzed the ratio  $r_A/r_B$  of adatom islands on Pt(111) using STM in a temperature range between 700 K and 925 K. Their result is in agreement with the results obtained in this work. One should emphasize though that Michely et al measured exclusively the ratio between the step free energies for A- and B-steps  $r_A/r_B$ . They did not determine the step free energies  $\beta_A$  and  $\beta_B$  as done in this work. As is shown in Fig. 4.4.3, we find that the ratio  $r_A/r_B$  depends on the temperature. For the highest temperature T = 713 K as considered in our study, we find  $r_A/r_B = 1.14 \pm 0.04$ .

This value is in agreement with the value  $1.15 \pm 0.03$  found by Michely et al. Considering the temperature trend as found in our data (Fig. 4.4.3) we propose that the result of Michely et al is not as exact as our data set. One may, however, not exclude that the decrease of  $r_A/r_B$  levels off for temperatures higher than 720 K. Since the island shape has to become rounder at higher temperatures it is, however, not very likely that the constant value of  $r_A/r_B = 1.15 \pm 0.03$  for temperatures between 700 K and 925 K is accurate.

From the theoretical calculations, the closest to the experimental results is the calculation by Feibelmann [30], using LDA (Local Density Approximation) calculations. This value is in agreement with our data within 5%. This small deviation can be obtained by the fact that the LDA calculations by Feibelman are performed for T = 0 K, whereas the experimental data were obtained for much higher sample temperatures, where step free energy must be lower due to phonon contributions to the entropy of the steps. Slightly higher values for the step free energies were determined by Boisvert et al [31], also by using LDA-calculations. Using EAM (Embedded Atom Method) calculations, Nelson et al [32] determined a step free energy of the B-step in close agreement with the value obtained in this work. However, their value for the step free energy of the A-step deviates significantly from our result. Therefore, one may assume that the good agreement for  $\beta_B$  is accidental. This is also confirmed by inspecting the ratio  $\beta_A/\beta_B$  as found by Nelson et al who obtain a ratio  $\beta_A/\beta_B$  close to one, which was not observed in any of the experimental studies.

Island decay 39

# **Chapter 5**

# Non-equilibrium phenomena

## 5.1 Island decay

In the previous chapter, we have seen that surface mass transport is very important when surfaces are in equilibrium. For instance, islands undergo equilibrium fluctuations around their equilibrium shape due to atomic diffusion processes at the island edge. In this chapter, mass transport on crystal surfaces relevant in non-equilibrium phenomena is considered. A particular non-equilibrium phenomena on crystal surfaces we are interested in is the decay of islands. The island decay may be dominated by various mass transport mechanisms. By studies of the island decay one may determine the dominant mass transport species on crystal surfaces, as well as the energy barriers, which are relevant for the atomic transport processes on the surface. In this chapter, we will discuss the decay of vacancy islands on Cu(100), which is found to be diffusion limited and the relevant transport species is identified as mono-vacancies in accordance with previous studies on adatom island decay on Cu(100).

#### 5.1.1 Chemical potential of two-dimensional islands

The local chemical potential  $\mu_i(\Theta)$  of an island depends on the local curvature  $K(\Theta)$  of the island perimeter as described by the generalized Gibbs-Thomson relation [33, 34]:

$$\mu_{i}(\Theta) = \Omega \ \widetilde{\beta}(\Theta) K(\Theta). \tag{5.1.1.1}$$

Here,  $\Omega = a_{\parallel} a_{\perp}$  ( $a_{\perp}$  is the atomic distance perpendicular to the step) is the area of an atom and  $\widetilde{\beta}$  is the step-edge stiffness. The step-edge stiffness is the energy necessary to elongate a rough step length. Its relation with the step free energy  $\beta$  is given by

$$\widetilde{\beta}(\Theta) = \frac{\partial}{\partial L} \int_{0}^{L} \beta(\Theta) ds \cong \beta(\Theta) + \frac{\partial^{2} \beta}{\partial \Theta^{2}}, \qquad (5.1.1.2)$$

where L is the step length. In general, the step energy  $\beta$  is a function of the angle  $\Theta$  (see Chapter 4). When the islands assume their equilibrium shape, the chemical potential is constant along the island perimeter. In this case,  $\mu_i(\Theta)$  is independent of  $\Theta$  and may be replaced by a constant chemical potential  $\mu_i$  for the entire island perimeter.

The theory of Ostwald ripening describes the island decay analytically. For simplicity, the surface is assumed to be isotropic. Then, the angle dependence of the step-edge stiffness disappears as well as the second term in equation (5.1.1.2). Hence,  $\widetilde{\beta} = \beta$  and the equilibrium shape of the island is a circle. The free energy of an island at constant temperature depends on the number of atoms in the island and on the length of the island perimeter. The number of atoms for a circular island with radius  $R_i$  is

$$N = \frac{1}{\Omega} \pi R_i^2.$$
 (5.1.1.3)

And the perimeter length is

$$P(N) = \sqrt{4\pi N\Omega} . (5.1.1.4)$$

Then, the free energy becomes

$$F(N) = U - TS = E_{ad} \cdot N + \tilde{\beta} \cdot P(N) - TS, \qquad (5.1.1.5)$$

where U is the inner energy,  $E_{ad}$  is the adatom creation energy from kinks onto the terrace<sup>1</sup> and S is the entropy. The former equation is valid in the next-neighbor model. In this model, the long range interactions are not taken into account. We may obtain the chemical potential  $\mu(N)$  of an island as a function of the number of atoms from (5.1.1.3) and (5.1.1.4). The derivation with respect to N (for T = const) yields

$$\frac{dF}{dN} = E_{ad} + \frac{\tilde{\beta} \cdot \sqrt{4\pi\Omega}}{2\sqrt{N}} = E_{ad} + \frac{\tilde{\beta}\Omega}{R_{i}} = E_{ad} + \mu_{circle}.$$
 (5.1.1.6)

The adatom creation energy  $E_{ad}$  is a constant for all island sizes.  $\mu_{circle}$  describes the contribution of the island perimeter to the chemical potential. This contribution depends on the island radius and it determines the island ripening on a surface. Although equation (5.1.1.6) is derived for a circular island, it holds also for hexagonal and quadratic islands [9, 35], when an additional shape factor  $\eta$  is used. The shape factor describes the relation between the given island to an equivalent circular island with radius R and the same area [9, 35]:

$$\mu_{i} = \mu_{circle} \cdot \eta = \eta \Omega \frac{\tilde{\beta}}{R},$$

$$\eta = \sqrt{\frac{2\sqrt{3}}{\pi}} \text{ (hexagonal)}, \quad \eta = \frac{2}{\sqrt{\pi}} \text{ (square)}$$
(5.1.1.7)

 $<sup>^1</sup>$  For simplicity, in the following  $E_{ad}$  is defined as the adatom creation energy. One should emphasize though that  $E_{ad}$  in a more general understanding represents the creation energy of the dominant transport species on the terrace. That is, in the case that mono-vacancies are the transport species,  $E_{ad}$  has to be replaced by  $E_{vac}$  (creation energy of mono-vacancies on the terrace).

#### 5.1.2 Theory of Ostwald ripening

With the help of equations (5.1.1.6) and (5.1.1.7) one can analyze the island decay for a system of islands. Lifshitz and Slyozov [36] and Wagner [37] described the theory for the ripening of small particles in colloidal liquids. Chakraverty [38] as well as Wynblatt and Gjostein [39] applied the theory to the decay of islands on surfaces. In the analytical theory of Ostwald-ripening, the starting point is a symplified island configuration of a circular adatom island inside a circular vacancy island (Fig 5.1.2.1). The same description works also for other combinations of adatom and vacancy islands, e.g. adatom island on top of an adatom island or vacancy island inside a vacancy island. Without restriction of generality, it is assumed that the mass transport is realized by

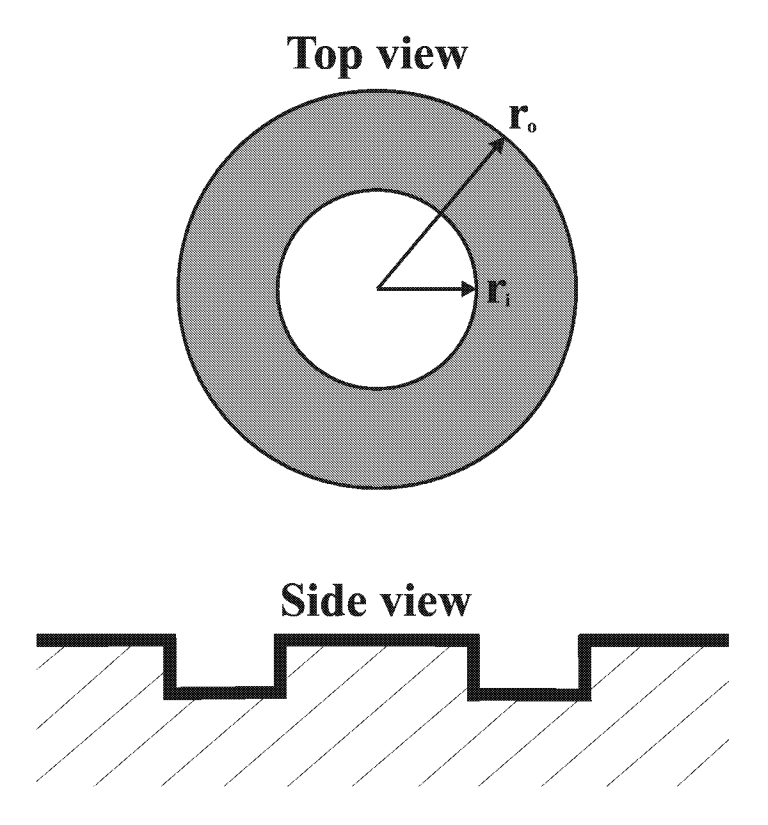


**Figure 5.1.2.1** *Schematic representation of the island configuration used to derive the Ostwald theory. See text for explanation.* 

adatom diffusion. As we will show later in section 5.1.3, where the experimental data for Cu(100) will be discussed, the theoretical description of island decay is analogous for surfaces, on which vacancies are the dominant diffusion species. From Equation (5.1.1.7) one finds that the chemical potential of a smaller island is larger, i.e. for an island configuration shown in Fig. 5.1.2.1, the chemical potential  $\mu_i$  of the inner adatom island is larger then the chemical potential  $\mu_o$  of the outer vacancy island. In order to reduce the free energy of the system, a current J of adatoms from the inner to the outer island perimeter is established. The adatoms detach from the inner island, diffuse across the terrace and attach to the outer island edge. In this case, both islands have attachment coefficients of equal size:

$$s := e^{-\frac{E_{att}}{kT}}.$$
 (5.1.2.1)

Here E<sub>att</sub> is the attachment barrier (see Chapter 2) at the island edge. For island configurations such as the simple case of an adatom island on top of another adatom island, the attachment coefficients may be different. This is due to the fact that the attachment at the outer island perimeter may be hindered by an additional energy barrier, the so-called Ehrlich-Schwoebel barrier [13], for hopping across steps.

In the following, the net current between inner and outer island is calculated under the assumption that the islands are in quasi-equilibrium [9]. In quasi-equilibrium, the number of atoms detaching from the inner island perimeter must be equal to the number of attaching atoms. The number of atoms per time unit attaching to the inner island is given by

$$j_{att} = -k\rho(r_i), \qquad (5.1.2.2)$$

where k is a rate constant and  $\rho(r_i)$  is the concentration of adatoms on the terrace in close proximity to the inner island radius  $r_i$ . The mass current  $j_{det}$  detaching from the island must be equal in quasi-equilibrium and the adatom concentration is equal to the equilibrium concentration of adatoms (Fig. 1.2.2). Hence,

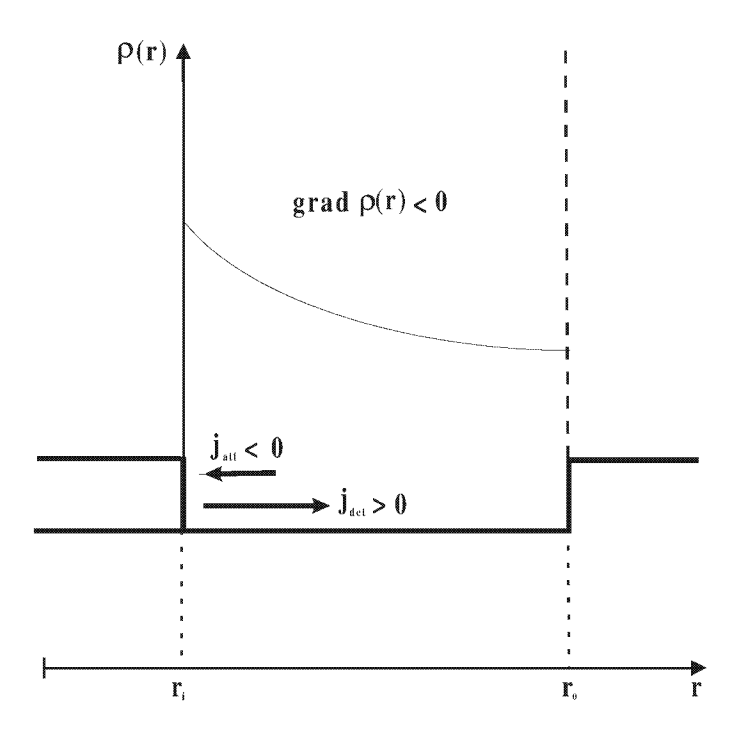


**Figure 5.1.2.2** Illustration to the derivation of the decay equations. The radii of the islands are measured from the center of the inner island. The detaching current is assumed positive and the attaching current is negative.

$$-j_{det} = -k\rho_{eq}(r_i) = j_{att}.$$
 (5.1.2.3)

Then, the net current j<sub>net</sub> is

$$j_{\text{net}} = j_{\text{det}} + j_{\text{att}} = k(\rho_{\text{eq}}(r_i) - \rho(r_i)).$$
 (5.1.2.4)

The net current must be equal to the terrace diffusion current j<sub>diff</sub>

$$j_{\text{net}} \stackrel{!}{=} j_{\text{diff}} = -v_{\text{diff}} a \operatorname{grad} \rho(r_i), \qquad (5.1.2.5)$$

where the constant "a" is given in atomic units and is related to the atomic distance between equivalent lattice positions on the terrace. The hopping rate on the terrace depends on the diffusion barrier  $E_{diff}$ ,  $v_{diff} = v_0 \exp(-E_{diff}/k_BT)$ . The sticking factor s is equal to the ratio between the sticking rate  $v_{stick} = v_0 \exp(-(E_{stick} + E_{diff})/k_BT)$  and the diffusions rate  $v_{diff}$  (Fig. 5.1.2.3),  $s = v_{stick}/v_{diff}$ . The rate constant k is the product of the hopping rate on the terrace and the additional sticking rate s,  $k = sv_{diff}$ . Then, the adatom concentration in equilibrium follows to be

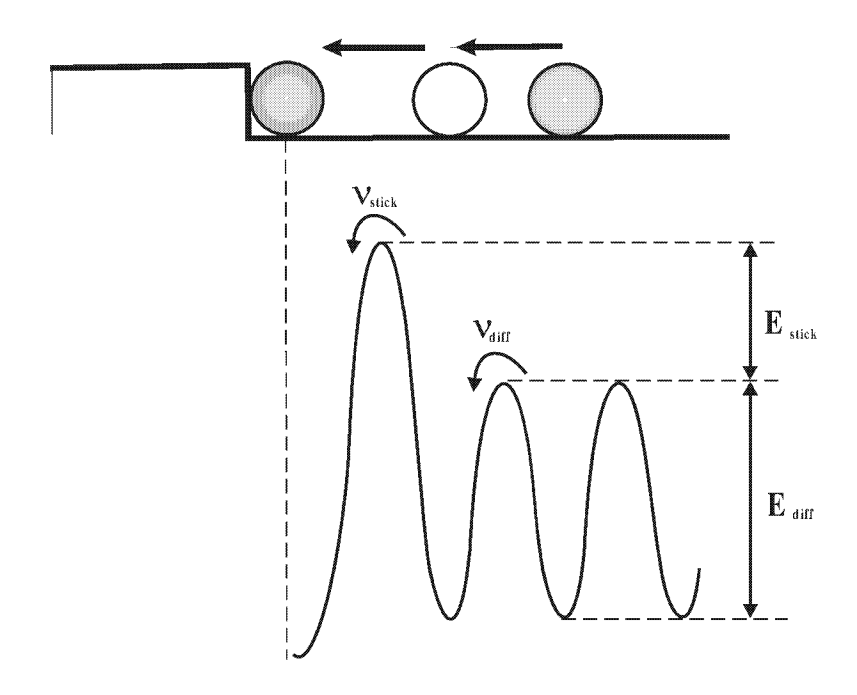


**Figure 5.1.2.3** *Model of the energy barrier for the sticking of an adatom at an island edge.* 

$$\rho(\mathbf{r}_{i}) - \frac{\mathbf{a}}{\mathbf{s}} \operatorname{grad} \rho(\mathbf{r}_{i}) = \rho_{eq}(\mathbf{r}_{i}). \tag{5.1.2.6}$$

The equation for stationary diffusion determines the local adatom concentration via the Laplace equation

$$\vec{\nabla} \cdot \vec{j}_{\text{net}} = -v_{\text{diff}} \ a \Delta \rho(\vec{r}) = \dot{\rho}(\vec{r}) = 0. \tag{5.1.2.7}$$

Here,  $\dot{\rho}(\vec{r})$  denotes the time derivative of  $\rho(\vec{r})$ .

The solution of equation (5.1.2.7) in polar coordinates is

46 \_\_\_\_\_ Chapter 5

$$\rho(\mathbf{r}_{i}) = \ln \left| \frac{\mathbf{r}_{i}}{\mathbf{r}_{o}} \right| \frac{\rho_{eq}(\mathbf{r}_{i}) - \rho_{eq}(\mathbf{r}_{o})}{\ln \left| \frac{\mathbf{r}_{i}}{\mathbf{r}_{o}} \right| - \frac{\mathbf{a}}{\mathbf{s}\mathbf{r}_{i}}} + \rho_{eq}(\mathbf{r}_{i}). \tag{5.1.2.8}$$

Note that vacancy islands have a negative curvature and the radius  $r_o$  is interpreted as negative variable. The net mass current is then

$$j_{\text{net}} = v_{\text{diff}} \frac{a}{r_{\text{i}}} \frac{\rho_{\text{eq}}(r_{\text{o}}) - \rho_{\text{eq}}(r_{\text{i}})}{\ln \chi + \frac{a}{\text{sr}_{\text{i}}}}.$$
(5.1.2.9)

Here, we set  $\chi = r_0/r_i$ . The reduction rate of the particles N with time is given by

$$\begin{split} \frac{dN}{dt} &= -j_{net} \, \frac{2\pi r_i}{a} \\ \frac{dN}{dt} &= 2\pi \nu_{diff} \, \frac{\rho_{eq} \big( r_i \big) - \rho \big( r_o \big)}{\ln \chi + \frac{a}{sr_i}} \end{split} \tag{5.1.2.10}$$

Then, the equilibrium concentration becomes

$$\rho_{\rm eq} = \rho_{\infty} \, e^{\frac{\mu(r_{\rm i})}{k_{\rm B}T}} = \exp \left\{ -\frac{E_{\rm ad}}{k_{\rm B}T} \right\} \exp \left\{ \frac{\eta \beta \Omega}{r_{\rm i} k_{\rm B}T} \right\}. \tag{5.1.2.11}$$

Using  $v_{\text{diff}} = v_0 \exp(-E_{\text{diff}}/k_B T)$  and the island area  $A = N\Omega$  in (5.1.2.11) we find

$$\frac{dA}{dt} = 2\pi v_0 \Omega \exp\left\{-\frac{E_{ad} + E_{diff}}{k_B T}\right\} \frac{\exp\left\{\frac{\eta \beta \Omega}{k_B T} \frac{1}{r_i}\right\} - \exp\left\{\frac{\eta \beta \Omega}{k_B T} \frac{1}{r_o}\right\}}{\ln \chi + \frac{a}{sr_i}}.$$
 (5.1.2.12)

Equation (5.1.2.12) can be solved for two limiting cases:

#### 1) Diffusion-limited island decay; s = 1:

For s =1, the detachment of atoms at the island edge is faster than the diffusion on the terrace and then, the rate constant is given by the diffusion rate on the terrace,  $k=v_{diff}$ . Using a linear expansion of the exponential function and with  $ln\chi >> a/r_i$  equation (5.1.2.12) becomes

$$\frac{dA}{dt} \approx \frac{2\pi v_0 \Omega^2 \eta \beta}{k_B T \ln \chi} exp \left\{ -\frac{E_{ad} + E_{diff}}{k_B T} \right\} \left( \frac{1}{r_i} - \frac{1}{r_o} \right). \tag{5.1.2.13}$$

By neglecting the time dependence of  $ln\chi$  (which may not necessarily be satisfied) and taking into account that  $r_o >> r_i$  it follows

$$\frac{dA}{dt} = \pi \frac{d(r_i^2)}{dt} \approx \frac{2\pi v_0 \Omega^2 \eta \beta}{k_B T \ln \chi} exp \left\{ -\frac{E_{ad} + E_{diff}}{k_B T} \right\} \frac{1}{r_i}$$
 (5.1.2.14)

or

$$r_i^2 \frac{dr_i}{dt} \approx \frac{v_0 \Omega^2 \eta \beta}{k_B T \ln \chi} exp \left\{ -\frac{E_{ad} + E_{diff}}{k_B T} \right\}. \tag{5.1.2.15}$$

Hence, the island decay rate in the diffusion-limited case is

$$A(t) \approx \left(\frac{3\pi^{\frac{3}{2}} v_0 \Omega^2 \eta \beta}{k_B T \ln \chi} \exp\left\{-\frac{E_{ad} + E_{diff}}{k_B T}\right\}\right)^{\frac{2}{3}} (t - t_0)^{\frac{2}{3}}.$$
 (5.1.2.16)

48 \_\_\_\_\_ Chapter 5

As a result, we find that if the diffusion on the terrace is slow and the sticking probability of atoms at the island edge is s = 1, the time dependence of the island area is proportional to  $t^{2/3}$ .

#### 2) Detachment-limited island decay; s<<1:

Here, the atom attachment/detachment at the island edge is slow compared to the diffusion on the terrace. Then,  $\ln\chi <<$  a/(sr<sub>i</sub>), r<sub>i</sub>/r<sub>o</sub> << 1 and using a linear expansion for the exponential functions as before one obtains

$$\frac{dA}{dt} \approx \frac{2\pi v_0 s\Omega}{ak_B T} exp \left\{ -\frac{E_{ad} + E_{diff}}{k_B T} \right\}, \qquad (5.1.2.17)$$

which means dA/dt ∝ const. Furthermore one gets

$$A(t) \approx \frac{2\pi v_0 s\Omega}{ak_B T} exp \left\{ -\frac{E_{ad} + E_{diff}}{k_B T} \right\} (t - t_0), \qquad (5.1.2.18)$$

i.e. the island area changes linearly in time.

Although the classical Ostwald theory is derived for the special configuration of concentric islands, equations (5.1.2.15) - (5.1.2.18) may be applied to different island configurations. This is demonstrated in the following section where the analysis of experimental island decay data is described.

#### **5.1.3** Island decay on Cu(100)

A representative image of the Cu(100) surface as used in experiment is shown in Fig. 5.1.3.1. The temperature is 323 K. Vacancy islands are regularly distributed on the surface. Due to the 4-fold symmetry of the Cu(100) surface islands are about quadratic in shape with round corners. For the analysis of the vacancy islands, a total of 49 different islands were studied in a temperature regime between 323K and 398K. The

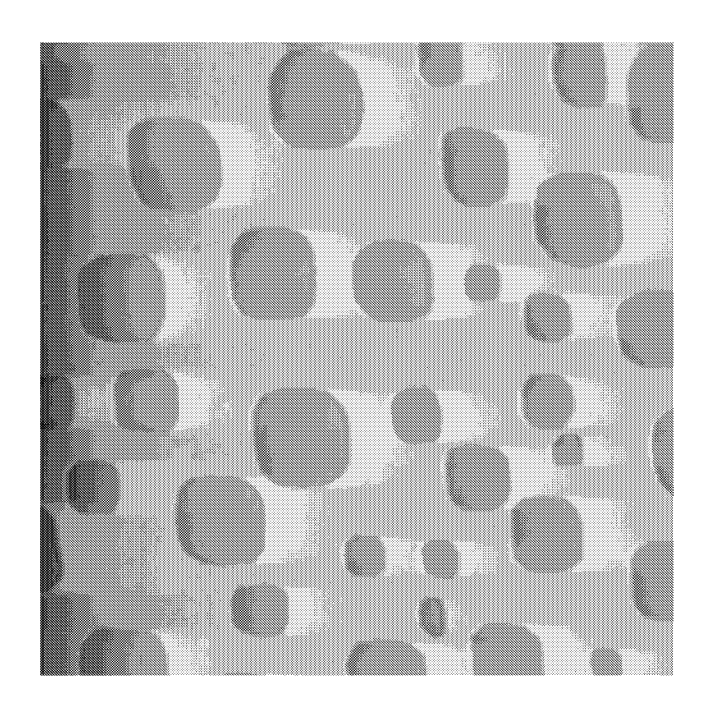


**Figure 5.1.3.1** Typical STM-image of the Cu(100) surface at 323K after sputtering to create vacancy islands. The scan width is 194.4 nm. The vacancy island shape reflects the four-fold symmetry of the surface.

decay of each of these islands was examined by measuring the island area in subsequent STM images. Typically 5500 STM images of were used for the analysis. The total time to record a STM image was t = 60 - 90s. For the analysis of the island decay, exclusively those islands were chosen which kept their shape close to the equilibrium shape, i.e. islands which merged with other islands for instance were not taken into account. Other islands, which reveal elongate shapes were also neglected since those shapes usually indicate the contamination of the island perimeter. When contamination

such as adsorbates is present at the island edge, the island perimeter is frequently locally pinned, the chemical potential of the island deviates from the equilibrium value. In this case, the decay rate of the island may deviate from the value that is supposed to be measured. Therefore, one must carefully check for whether island edges show indication of pinning.

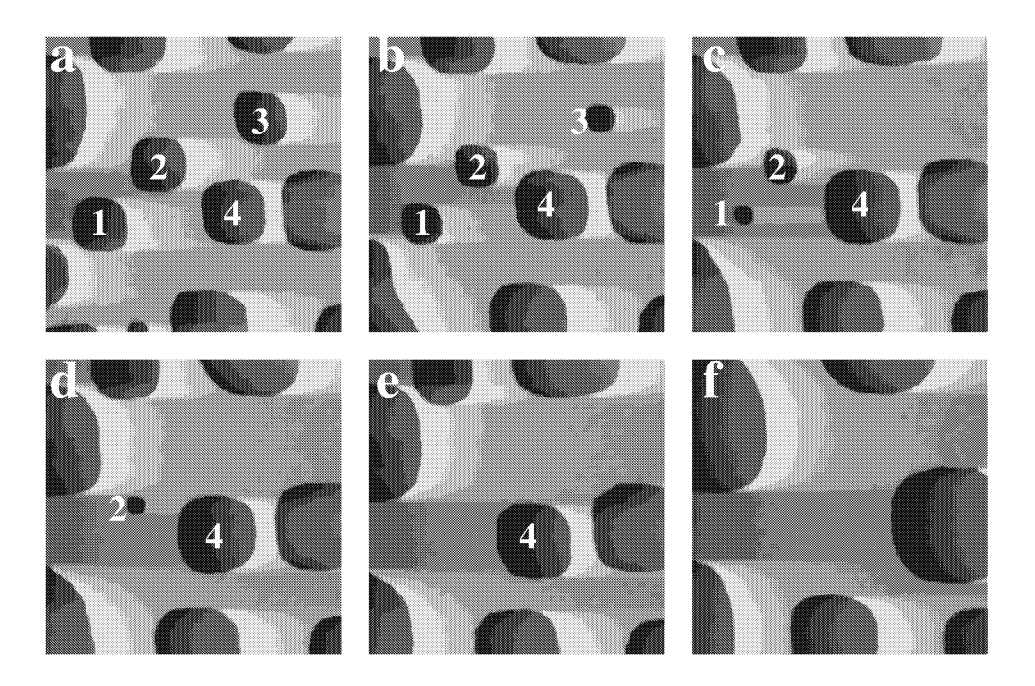


**Figure 5.1.3.2** The evolution of vacancy islands on Cu(100) with time at 353K. For all of the STM-images the scan width is 97.2 nm. The recording time of the images are as follows a) 0s, b) 1540s, c) 2145s, d) 2530s e) 3355s f) 8085s.

In the following analysis of vacancy island decay on Cu(100), we apply the classical Ostwald-theory to the case of a large ensemble of monolayer deep vacancy islands on the surface. The configuration of an ensemble of islands deviates significantly from the one assumed in the classical Ostwald theory (see also Fig. 5.1.2.1). Therefore, some assumptions have to be made for the following analysis. Instead of a constant concentration of mass carriers  $\rho_0$  at the outer island perimeter, an appropriate screening length is introduced, which encloses a region around the island with an average concentration  $\langle \rho \rangle$  of mass carriers on the terrace [17, 40, 41]. This screening length is not explicitly defined and depends on the island radius. When the screening areas of adjacent islands do not overlap, the island configuration can be interpreted as an ensemble of isolated islands on the terrace. In this case, the island

decay equations (5.1.2.16) and (5.1.2.18) can be directly applied for the decay analysis of an ensemble of islands. When the screening regions overlap, there will be a mass current from small islands to the large ones.

In Fig. 5.1.3.2, the evolution of four vacancy islands on Cu(100) at 353K (indicated with numbers 1 – 4) is shown. Initially, the islands 1-3 have almost the same size and island 4 is slightly bigger. Up to t=500s all four islands decay (see also Fig. 5.1.3.3). Whereas islands 1-3 decay monotonically and eventually vanish around t=2500-3000s, island 4 grows after t=500s. The arrows in Fig. 5.1.3.3 indicate sudden 'jumps' in the area of island 4 at the points in time where the islands 1, 2 and 3 are in their final state of decay. Island 4 continues its decay eventually around t=3000s after islands 1-3 have disappeared. Hence, island 4 obviously has gathered a significant amount of the total mass currents from islands 1-3.

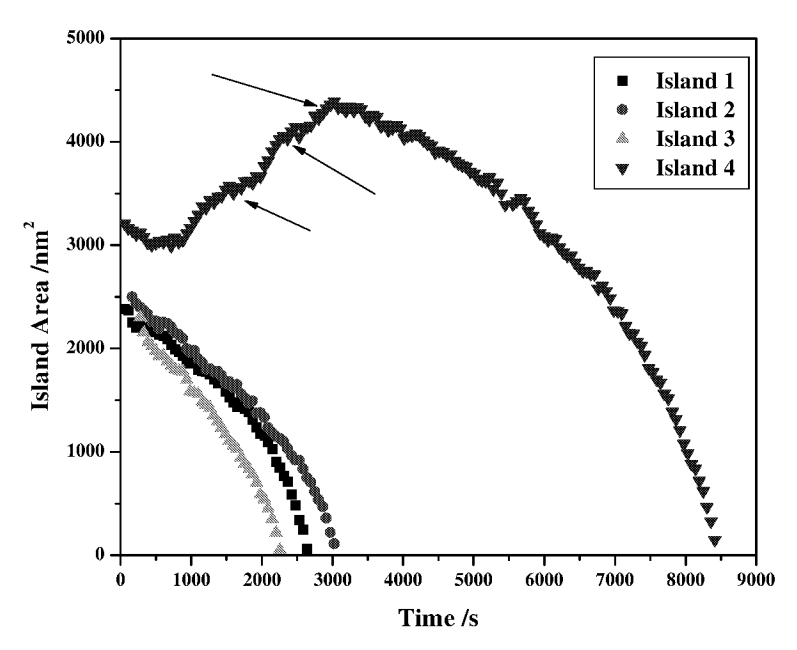


**Figure 5.1.3.3** Decay curves of vacancy islands on Cu(100) at 353K. The arrows show the points in time when the islands 1, 2 and 3 are in their final state of decay and island 4 grows rapidly.

According to the decay curves in Fig. 5.1.3.3, the island decay is not linear in time. Hence, it is reasonable to assume that the island decay is diffusion limited. This may be verified by fitting the decay curves of the islands according to equation (5.1.2.16). Due to the influence of surrounding islands on an individual decay curve, the

fitting of a measured decay curve is not a trivial task. In the last phase of the decay, the islands are small (with high chemical potential) and the decay curves are close to a

power law in time. The decay curves were fitted to a power law 
$$A(t) = A_0 \left(1 - \frac{t}{t_0}\right)^m$$

with free parameters  $A_0$ ,  $t_0$  and m. The measured values for different temperatures are presented in Tables 5.1.3.1-4. From the tables, one can see that the measured exponents are around m  $\approx 0.66 = 2/3$ . Only for the highest temperature T=398K, the deviation of the measured exponent from the theoretical value 2/3 is larger.

The measured values of m are close to the theoretically expected value for diffusion limited decay (see equation (5.1.2.16)). From equation (5.1.2.14) one gets for the time derivative of the island area for a distinct island area  $A^*$ :

$$\ln \frac{dA}{dt}\Big|_{A^*} = -\frac{E_{ad} + E_{diff}}{k_B T} + \ln \left(\frac{2\pi v_0 \Omega^2 \eta \beta}{k_B T \ln \chi} \frac{1}{\sqrt{A^*}}\right). \tag{5.1.3.1}$$

The measurements were performed in a temperature interval between 323K and 398K. In this interval, the second term on the right hand side of the equation (5.1.3.1) may be assumed to be constant. Then, the slope of the Arrhenius plot  $\ln A'(T)|_{A^*}$  corresponds to the energy  $E_{ad}+E_{diff}$ .

In order to determine the slope of the decay curve for a distinct island area  $A^*$ , the decay curves were fitted with a function  $A(t) = -c \cdot (t_0 - t)^m$ , with parameters c,  $t_0$  and m. The time  $t^*$  corresponds to the island area  $A^*$ , i.e. the time  $t^*$ , when the island has a size  $A^*$ , is  $t^* = t_0 - \left(A^*/c\right)^{1/m}$ . The time derivative of A(t) at  $t = t^*$  is

**Table 5.1.3.1** Decay exponent for vacancy island decay on Cu(100) at T=323K.

Island number	m	
1	0.73	±0.03
2	0.64	±0.02
3	0.77	±0.14
4	0.67	±0.03
5	0.62	±0.02
6	0.65	±0.03
7	0.66	±0.01
8	0.67	±0.02
9	0.63	±0.01
10	0.59	±0.07
11	0.57	±0.01
12	0.69	±0.01
13	0.60	±0.01
14	0.62	±0.02
15	0.68	±0.01
16	0.70	±0.01
17	0.66	±0.01
18	0.67	±0.01
19	0.64	±0.01
20	0.71	±0.01
Average	0.66	±0.05

**Table 5.1.3.2** Decay exponent for vacancy island decay on Cu(100) at T=353K.

Island number		m
1	0.66	±0.02
2	0.60	±0.01
3	0.65	±0.01
4	0.58	±0.01
5	0.63	±0.02
6	0.59	±0.01
7	0.65	±0.01
8	0.67	±0.02
Average	0.63	±0.03

54 \_\_\_\_\_ Chapter 5

**Table 5.1.3.3** Decay exponent for vacancy island decay on Cu(100) at T=363K.

Island number		m
1	0.65	±0.65
2	0.76	$\pm 0.04$
3	0.60	±0.10
4	0.69	$\pm 0.02$
5	0.66	$\pm 0.02$
6	0.57	±0.18
Average	0.66	±0.07

**Table 5.1.3.4** Decay exponent for vacancy island decay on Cu(100) at T=398K.

Island number		m
1	0.55	±0.07
2	0.42	±0.03
3	0.43	$\pm 0.06$
4	0.41	±0.01
5	0.73	±0.13
6	0.57	±0.03
7	0.54	±0.04
8	0.62	±0.01
9	0.57	$\pm 0.02$
10	0.57	±0.03
11	0.57	±0.02
12	0.48	±0.61
13	0.55	±0.03
14	0.72	±0.07
15	0.59	±0.03
Average	0.56	±0.09

$$A'|_{A^*} = -cm \left(\frac{A^*}{c}\right)^{\frac{m-1}{m}}.$$
 (5.1.3.2)

In the experimental analysis, the fitting of the island decay curves faced severe problems: Small islands decay very fast and the STM cannot acquire enough images for the decay curve to be fitted with appropriate accuracy [17]. Large islands are influenced by the surrounding islands (see island 4 in Fig. 5.1.3.3) and cannot be fitted over the entire duration of their decay. As optimum value an island area of  $A^*$ =1000 atoms was chosen. Islands on Cu(100) with that size at temperatures between 323K and 398K appear to be small enough not to be influenced by the surrounding islands. Furthermore, islands with a size of about 1000 atoms are large enough, so that their decay curves can be fitted properly. Changing the value of  $A^*$  by  $\pm 500$  atoms does not change the result significantly. Fig. 5.1.3.4 shows the Arrhenius plot of  $dA/dt|_{A^*}$ . The data points may be fitted by a straight line and the slope of the curve corresponds to an energy of  $E_{ad}+E_{diff}=0.73\pm0.124$  eV.

The results presented in this section, namely the decay rate exponent m=0.66 and the fact that the decay of the larger islands is influenced by the decay of the smaller islands, show that the decay of vacancy islands on Cu(100) is diffusion limited. From the experimental study presented here it becomes obvious that the Ostwald-theory may be applicable to an ensemble of monoatomic deep vacancy islands on the terrace, however, exclusively in the late state of the decay when the islands are smaller, when their chemical potential is larger and when they are not influenced by surrounding islands. The exponent m of the decay curves is in agreement with the value 2/3 derived in the Ostwald theory except for the highest of the studied temperatures T=398K where a slightly smaller value is found (see tables 5.1.3.1-5.3.1.4). This may be due to the larger time of 90 s (compared to 60 s) used for the STM recording of a single image. This leads to a smaller number of measured points in the decay curve for the late stage of the decay, when the islands decay faster. Therefore, the point in time, when the islands eventually vanish can be determined merely with an accuracy of about  $\pm 45$  s. It

turns out that the small shift in the time where the island vanish may have a strong influence on the measured decay exponent.

One may compare the results presented here with investigations by Hannon et al [40]. These authors studied the decay of adatom islands on Cu(100) and found that the

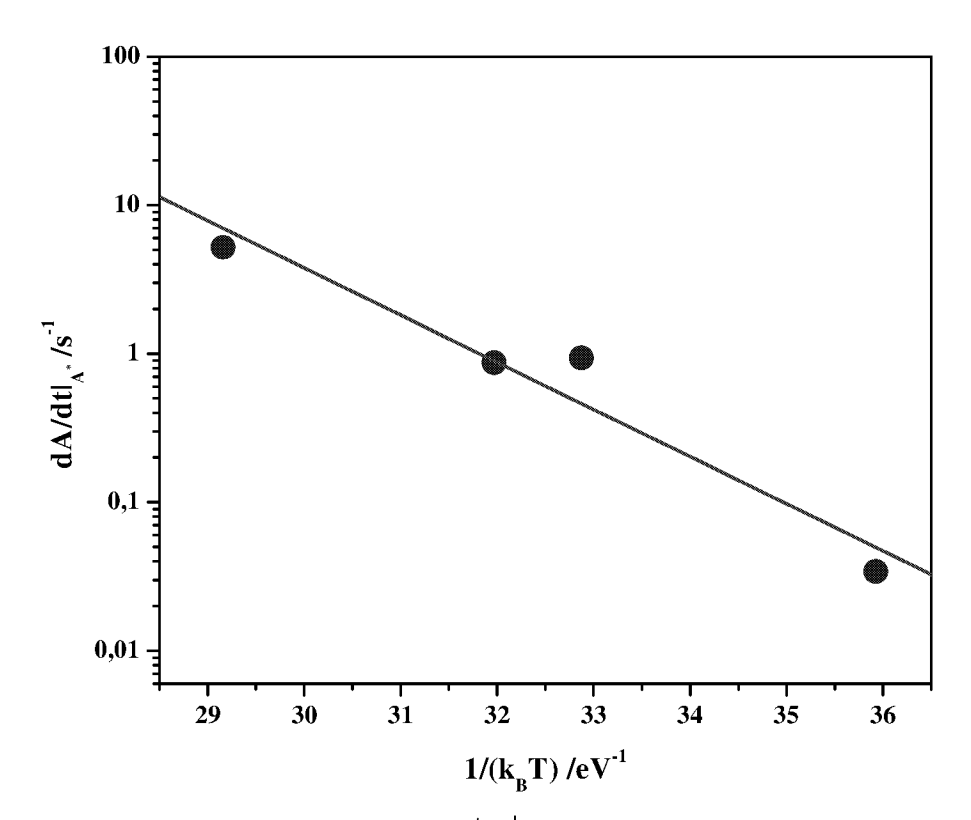


**Figure 5.1.3.4** Arrhenius plot of  $dA/dt|_{A^*}$  for vacancy islands with an area of  $A^* = 1000$  atoms at temperatures between 323K and 398K. The slope of the fitting line corresponds to the energy of 0.73 $\pm$ 0.12eV.

decay of adatom islands on Cu(100) is detachment limited. They showed furthermore that the island decay on Cu(100) is dominated by the diffusion of mono-vacancies on the Cu(100) surface, which serve as dominant mass transport carriers. This result is confirmed by the study presented here: If adatoms were the dominant transport species, it would be reasonable to assume that the attachment-detachment barrier at the vacancy island edge would be high compared to the diffusion barrier on the terrace because the adatoms have to hop over the step edge of the vacancy island. In the case of adatom island decay, the attachment-detachment barrier should be low compared to the diffusion barrier, if adatoms were the transport species. Hence, one would expect that the decay of adatom islands were diffusion limited and that the decay of vacancy islands

were detachment limited. The opposite is observed in experiment: On Cu(100), adatom island decay is detachment limited [40] and vacancy island decay (as presented in this work) is diffusion limited. This can be explained only if one assumes that monovacancies in the terrace are the dominant transport carriers. For mono-vacancies, it is reasonable to assume that the attachment-detachment barrier at vacancy island edges is low (compared to the diffusion barrier on the terrace). The attachment barrier for monovacancies at adatom island edges may be expected to be higher than at vacancy island edges. In fact, from our measurements we can deduce an estimate for this attachment barrier E<sub>att</sub>. Comparing our results for the activation energy with equation (5.1.3.1) shows that  $E_{vac} + E_{diff} = 0.73 \pm 0.12$  eV, where the adatom creation energy is now replaced by the vacancy formation energy E<sub>vac</sub>. Klünker et al. [41] measured an activation energy for adatom island decay on Cu(100) of  $0.80 \pm 0.03$  eV. Because adatom islands decay detachment limited on Cu(100), this activation energy corresponds to the sum  $E_{att} + E_{vac} + E_{diff}$  (equation (5.1.2.18)). Using  $E_{vac} + E_{diff} = 0.73$  $\pm$  0.12 eV as determined in this thesis, one finds  $E_{att} \approx 0.1$  eV, which is in accordance with the conclusions by the Klünker et al [41].

The value for  $E_{vac}+E_{diff}=0.73\pm0.12~eV$  may also be compared with EAM (Embedded Atom Method) calculations by Karimi et al [42], who find  $E_{vac}+E_{diff}=0.83~eV$  and with MD (Molecular Dynamics) simulations by Merikoski et al [43] who obtain  $E_{vac}+E_{diff}=0.69~eV$ . Both values differ slightly from our experimental result, however, they are within the experimental error.

### 5.1.4 Rapid island decay

In addition to the island decay described by the classical Ostwald theory, the observation of another phenomenon called the rapid island decay was reported. During rapid island decay, islands decay much faster than expected for an island of distinct size in a specific environment at a given temperature. The rapid island decay is observed, if an island on top of another island or a monoatomic high island in close proximity to an infinite downward step approaches the lower step edge. The first observation of the fast island decay was reported by Giesen et al [44, 45]. In that work, the authors discussed the decay of an adatom island on top of another adatom island on a Cu(111) surface. More recently, rapid decay was also reported for Ag(111) by Giesen et al [10] and Morgenstern et al [46, 47] where it was demonstrated that not only adatom but also vacancy islands undergo rapid island decay. By studying coalescence induced fast island decay Giesen [48] could show that the decay rate during rapid island decay may significantly depend on the distinct island configuration and island environment. Since initially, rapid island decay was exclusively found for fcc(111) surfaces where an Ehrlich-Schwoebel barrier (ES-barrier) is known to exist at step edges [49-53], first microscopic explanations for the onset of rapid island decay were based on the presence of the ES-barrier: Giesen et al [44, 45] proposed a model where the Ehrlich-Schwoebel barrier disappears whenever the top island approaches the step edge below a critical distance w<sub>c</sub>. Supported by observations of Li et al [54] the initial model was based on the assumption that step edge on Cu(111) and Ag(111) surfaces serve as infinitely high barriers for the electrons in surface states. When the island edge distance becomes smaller than a critical distance w<sub>c</sub>, the surface state would be depopulated. Kevan and Gaylord [55, 56] published detailed data on the surface states and their temperature dependence for Cu(111) and Ag(111). Using their data, Giesen et al calculated the critical distance w<sub>c</sub> when the surface states are depopulated as a function of temperature. The measured temperature dependence of w<sub>c</sub> for Cu(111) was in excellent agreement with the prediction of the model. The data for Ag(111), however, deviated significantly, such that the model for rapid island decay based on a vanishing of the ES-barrier was proven to fail [10].

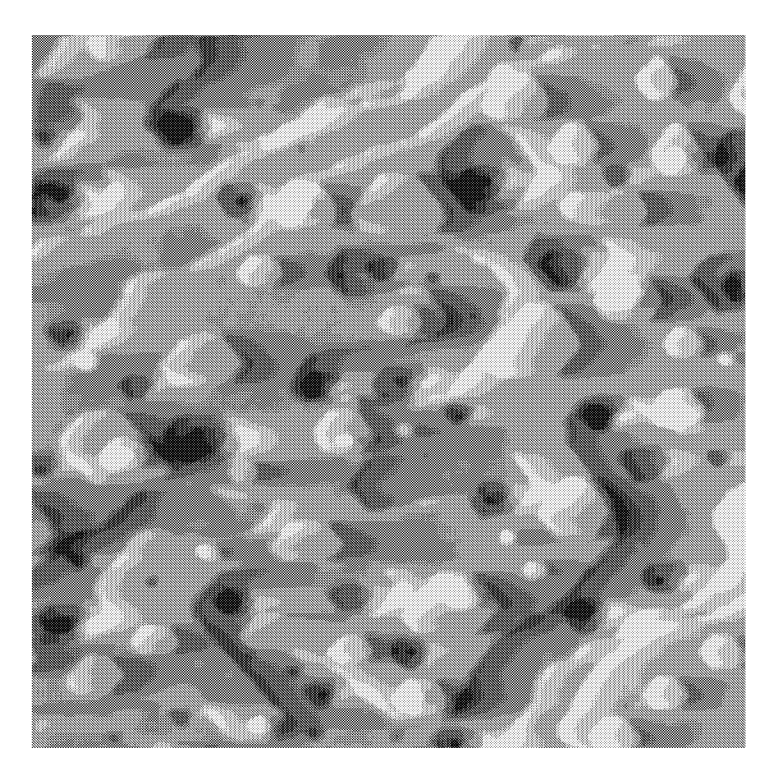


**Figure 5.1.4.1** STM-image of a Pt(111) surface at 513K. The scan width is 97.2 nm.

The key idea to extend experimental investigations to Pt(111) was to check whether rapid island decay was influenced by electronic effects at all: Whereas the electron energy bands for Cu(111) and Ag(111) are quite similar, they are very different for Pt(111). In this work, the study of fast island decay on Pt(111) is presented. In order to observe this phenomenon, multilayer adatom and vacancy islands were prepared by sputtering as described in Chapter 3. A typical image of the Pt(111) surface after preparation is shown in Fig. 5.1.4.1. In the image, one can see multilayer adatom and vacancy islands, as well as islands close to step edges. A configuration of a monoatomic high island in close proximity to downward step is shown in the STM-images in Fig 5.1.4.2. Initially (t = 0 min), the size of the island (indicated by the arrow) is almost stable (at 513K, the decay rate of islands on Pt(111) is about v=0.001 atoms/s). Due to island perimeter fluctuations, the island diffuses across the surface in a Brownian-like motion and the cluster eventually approaches the edge of the step (t = 20 min). Then, the rapid island decay sets in, the decay rate increases significantly and the island size decreases obviously with a higher rate (t = 40 min). In the STM images shown in Fig.

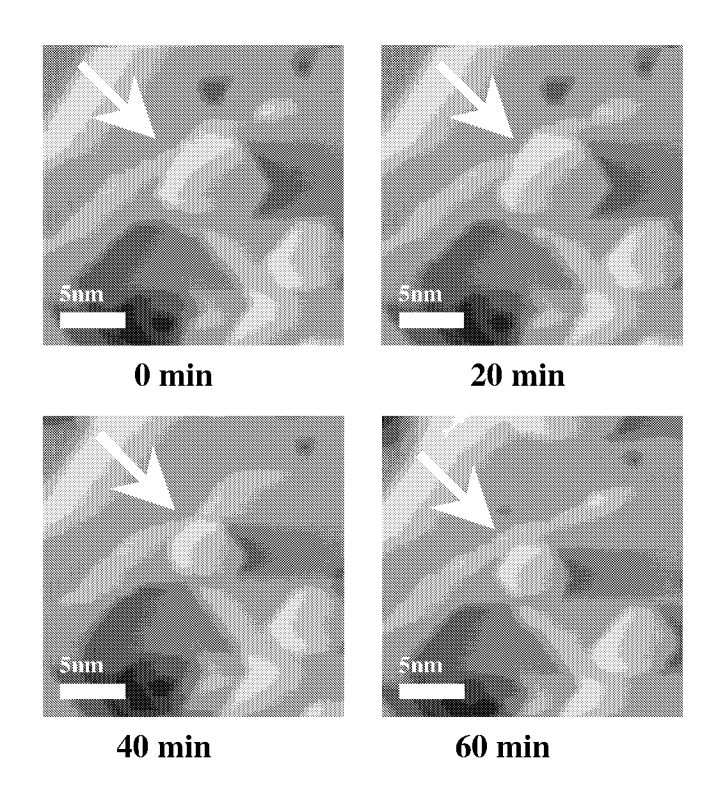


**Figure 5.1.4.2** STM-images of an adatom island on Pt(111) surface at 353K. See text for comments.

5.1.4.2, the process of fast island decay eventually comes to an end when the island moves away from the step edge and continues its decay with the initial rate (t = 60 min). In Fig. 5.1.4.3, the island area is plotted versus the time. The arrows indicate the points in time when the fast island decay sets in, respectively comes to an end, corresponding to the island status as shown in Fig. 5.1.4.2 at t = 20 min and t = 40 min. In the time interval in between, the decay rate increases from  $\nu = 0.001$  to  $\nu = 0.019$  atoms/s. As was discussed previously for Cu(111) and Ag(111) [10, 44, 45], the fast island decay sets in when the island approaches the lower step edge and the distance becomes smaller than a critical distance  $w_c$ . In Fig. 5.1.4.4, the measured critical distance  $w_c$  between the island edge and the step edge during the fast island decay process on Pt(111) is shown. From Fig 5.1.4.4 one finds that the distance remains constant and that  $w_c = 4.37$  a<sub> $\perp$ </sub> (here, a<sub> $\perp$ </sub> is the distance between two dense packed rows on the crystal surface) during the entire fast decay process.

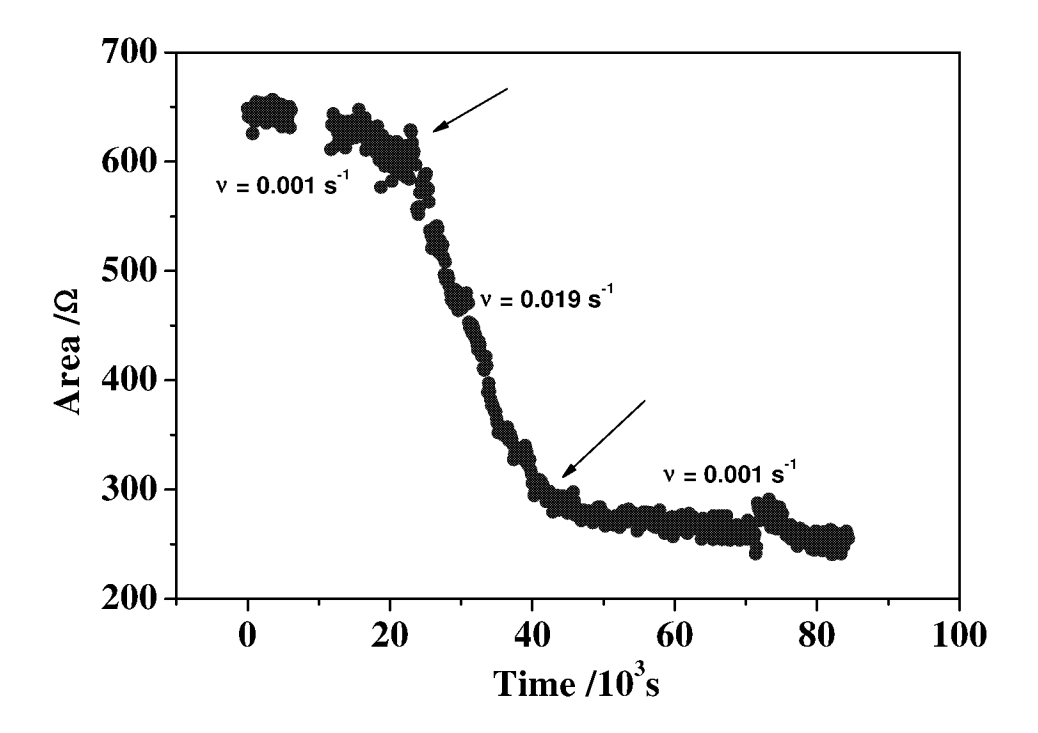


**Figure 5.1.4.3** Decay curve of the adatom island on Pt(111) shown in Fig 5.1.4.2 demonstrating the effect of the rapid island decay. The arrows indicate the points in time when the island approaches the step edge and when it moves away again. In the time interval in between, the island decay rate is higher by one order of magnitude.

The atomic mechanism responsible for the fast island decay is still under debate. Giesen et al [44, 45] initially proposed that the Ehrlich-Schwoebel barrier vanishes when the edge distance becomes smaller then  $w_c$  due to the depopulation of the surface state. They furthermore proposed that in this case, the critical distance for Pt(111) would be  $w_c = 8.75$  Å. In this work, the measured value of  $w_c$  for Pt(111) is  $w_c = 4.37$   $a_{\perp} = 10.49$  Å. This value is slightly larger, however, in reasonable agreement with the previously proposed value of 8.75 Å [45]. One should furthermore emphasize that for Pt(111), fast decay events were not as frequently observed as on Cu(111) and Ag(111). Hence, the value of  $w_c = 4.37$   $a_{\perp} = 10.49$  Å is obtained from one particular fast decay event. Hence, the error bar of 0.05Å has no statistical relevance and the real value for  $w_c$  (if averaged over many individual fast island decay events) could significantly deviate from 4.37  $a_{\perp}$ . A further study which could not be performed in this thesis was the

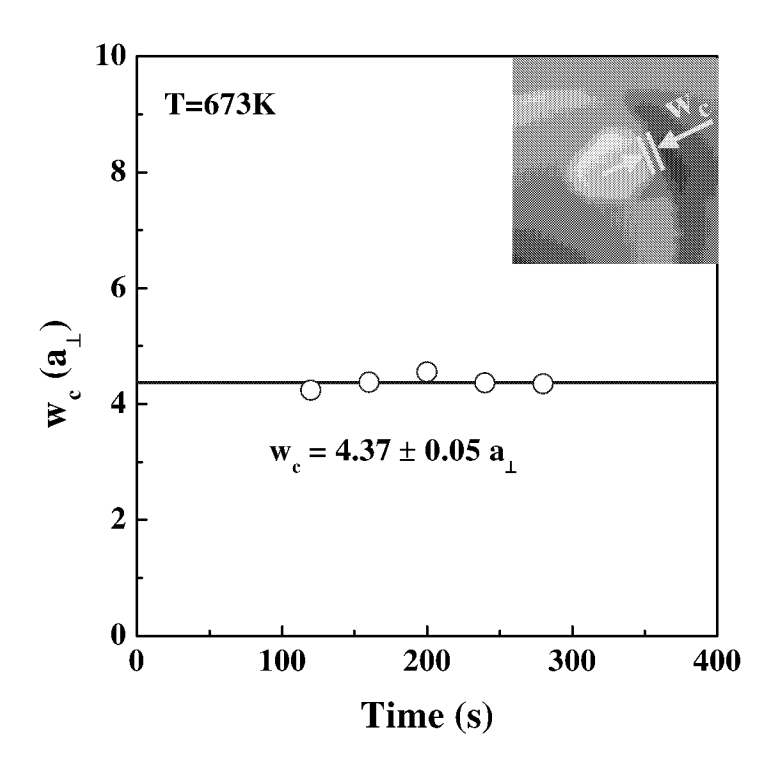


**Figure 5.1.4.4** Distance between the island and the step edge during the rapid island decay.

investigation of the temperature dependence of  $w_c$ . Giesen et al [10] showed that for Cu(111) and Ag(111)  $w_c$  was independent of the temperature. At least in the case of Ag(111), this result is in contradiction with the earlier proposed model of a vanishing of the ES-barrier due to a depopulation of the surface state.

Due to lack of time we were also not able to check in more detail whether the most recently discussed exchange mechanism for rapid island decay is in accordance with the observed decay event on Pt(111). Bartelt was the first to propose [57] that an exchange mechanism at island edges in close proximity could be the reason for rapid island decay. Later, such an exchange process was described in more detail by Giesen et al [10] and Morgenstern et al [47]. The proposed mechanism by Giesen et al is shown in Fig 5.1.4.5. Whenever the distance between the upper island edge and the lower edge becomes smaller than two atomic rows and, simultaneously, kinks in the upper and the lower edge are in close proximity, an exchange process between the kink atoms (atoms 1-3 in Fig. 5.1.4.5) should occur. Giesen et al could show [10] that all rapid decay

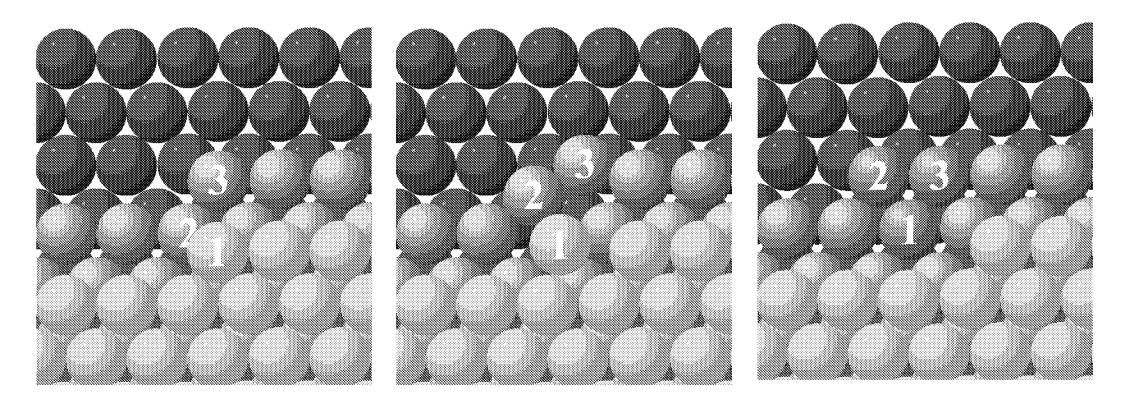


**Figure 5.1.4.5** Model of the microscopic process during rapid island decay as proposed by Giesen et al [10]. The atom (indicated with "1") merges from the kink site in the upper island edge into the kink site of the lower level edge via an exchange mechanism. In this exchange process, at least three atoms are involved.

events observed so far on Cu(111) and Ag(111) could be quantitatively described assuming this model. It is unfortunately still left to future work to check whether this exchange model could also explain all rapid decay events on Pt(111).

## **5.2 Island Coalescence on Cu(100)**

#### 5.2.1 Introduction to island coalescence and theoretical aspects

A number of studies show that on some metal surfaces Ostwald ripening is not the dominant coarsening process. Instead, another ripening mechanism plays the significant role – the dynamic coalescence of islands. In this process, two islands diffuse on the surface and eventually merge to form a new and bigger cluster. The island coalescence of adatom islands on Cu(100) was previously studied by Zuo et al [58] and Pai et al [59]. They showed that the island coalescence is the dominant coarsening mechanism on Cu(100). Wen et al [60], Pai et al [59] and Cadilhe et al [61] provided studies on Ag(100) and demonstrated that the coalescence is also the most frequently observed ripening process on this surface. Island coalescence as the dominant coarsening process on Ni(100) was reported by Hoogeman et al [62]. On some surfaces, Ostwald ripening may be the dominant coarsening mechanism, island coalescence may, however, be frequently observed such as on Ag(111) and Cu(111). A detailed description of island coalescence on Ag(111) was published by Eßer et al [63] and Rosenfeld et al [64].

In this work, a detailed analysis of the dynamic coalescence of vacancy islands on Cu(100) is used to determine the dominant mass transport mechanism along step edges on Cu(100) and to measure the relevant activation energy involved. Fig. 5.2.1.1 shows a sequence of STM images where an island coalescence process on Cu(100) is displayed. The process of island coalescence is divided into three time regions: First, the islands diffuse towards each other, eventually touch each other and form a neck-like connection (t = 0 min). The neck is characterized by regions of large positive curvature in the island perimeter, which generates a positive chemical potential in these regions. The chemical potential of the island perimeter outside the neck region is negative. The difference between positive and negative chemical potential in the two perimeter regions causes a large diffusion current from the regions with positive curvature to the regions with negative curvature. In the second phase, the positive curvature in the neck

region decreases until the curvature is zero and an oblong shape is formed (t = 110 min). Finally, the curvature along the entire island perimeter is negative, the gradient in chemical potential is smaller and the diffusion is slower. Then, the island shape eventually assumes, however slowly, its equilibrium shape (t = 220 min).

In order to quantitatively describe a process as shown in Fig. 5.2.1.1, one has to make use of a theory of island coalescence which is frequently discussed in literature.

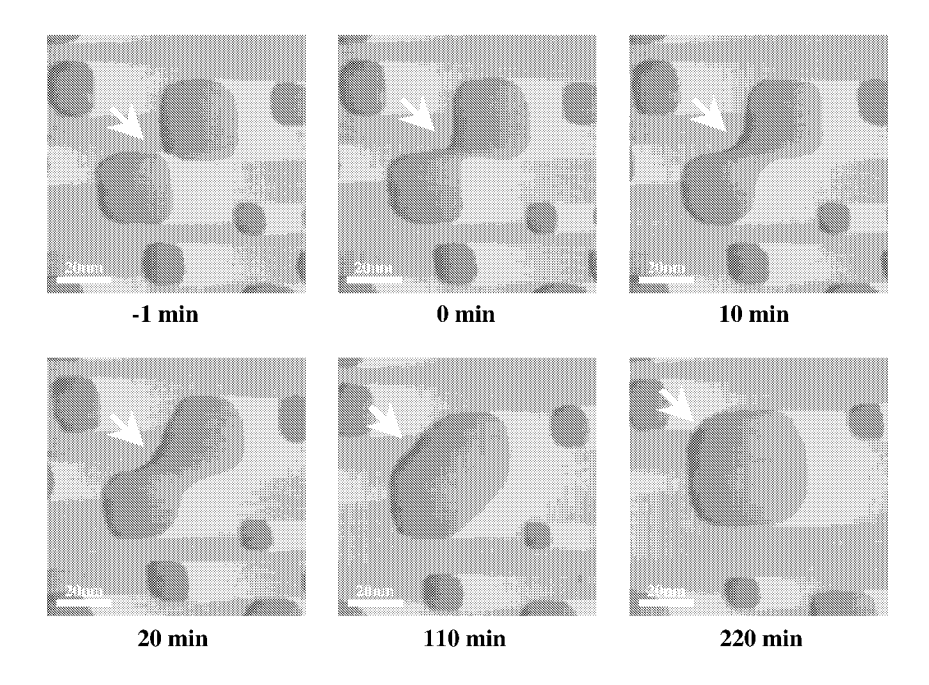


**Figure 5.2.1.1** The dynamic coalescence of two vacancy islands on Cu(100) at 323K. At time -1 min, the islands are still separated. At 0 min, both islands have merged and form a new cluster with a neck in the middle. 10 and 20 min: the neck width increases due to the large gradient of the chemical potential along the island perimeter. At 110 min, an oblong shape is formed, the island slowly changes to its equilibrium shape around 220 min.

The first theoretical explanation was given by Smoluchowski in 1916 [65, 66]. Therefore, surface coarsening via island coalescence is also called Smoluchowski ripening. Smoluchowski described the behavior of small particles in a colloidal solution. A similar theoretical description was published by Meakin in 1990 [67]. Using the continuum theory, a detailed theoretical explanation of the relaxation process of an island shape far from equilibrium, was given by Nichols and Mullins [68, 69]. A comprehensive discussion of the diffusion processes during island coalescence and during cluster diffusion was published by Khare, Bartelt and Einstein [8, 70]. They

showed that in the continuum limit the same atomic processes which are involved in equilibrium step fluctuations are responsible for adatom and vacancy island diffusion as well as for the relaxation of non-equilibrium cluster shapes.

In the following, we will first describe theoretically the step fluctuations of the island edge region with positive curvature. The step correlation function G(y,t) is a measure for the step fluctuations. G(y,t) is defined as [9]

$$G(y,t) = \langle (x(y,t) - x(y_0,t_0))^2 \rangle,$$
 (5.2.1.1)

where the coordinates x, y are defined as in Fig. 5.2.1.2 G(y,t) measures the fluctuation amplitude of the wandering step in space and time and it can be expressed in a Fourier representation for the spatial coordinate x [9]:

$$x(y,t) = \int_{q} x_q(t)e^{iqy}dy, \qquad q = \frac{2\pi n}{L_y}.$$
 (5.2.1.2)

Here,  $L_y$  is the length of the island edge region with positive (as denoted in Fig. 5.2.1.2) curvature and q is the wave number. Using equation (5.2.1.2), one can write the correlation function in a Fourier representation [9, 71]

$$G_{q}(t) = \langle |x_{q}(t) - x_{q}(0)|^{2} \rangle.$$
 (5.2.1.3)

From equations (5.2.1.2) and (5.2.1.3) one obtains for  $G_q(t)$  [26, 71-73]

$$G_{q}(t) = A(q)(1 - e^{-|t|/\tau(q)}).$$
 (5.2.1.4)

A(q) is the amplitude of the fluctuations and  $\tau(q)$  is the relaxation time. A(q) is inverse proportional to the step stiffness  $\tilde{\beta}$  [74]

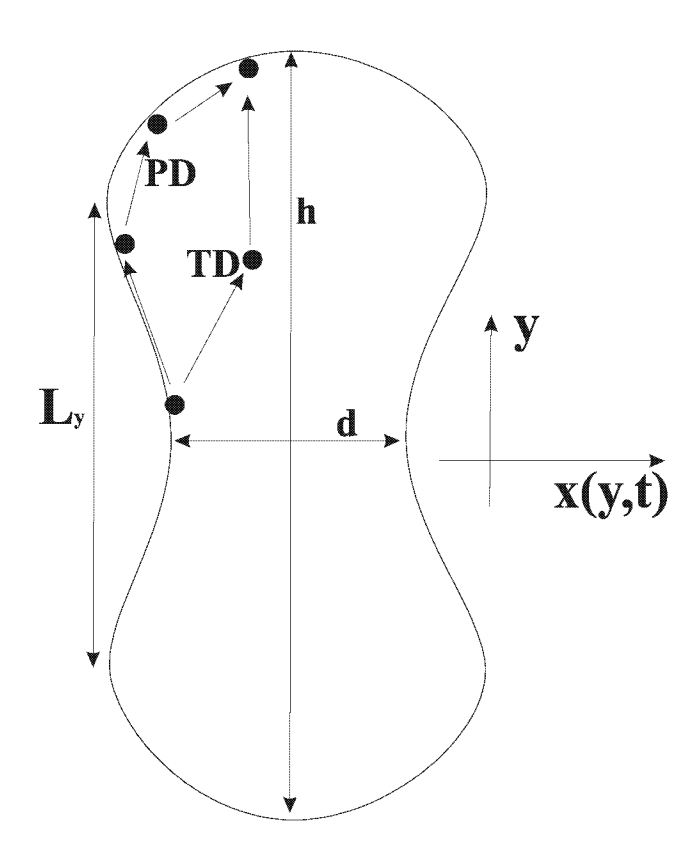


**Figure 5.2.1.2** Schematic presentation of the nomenclature used for the definition of the correlation function and for the diffusion processes involved in the relaxation of an island after coalescence. TD – diffusion over the terrace and PD – diffusion along the island perimeter.

$$A(q) = \frac{2k_B T}{L_y \widetilde{\beta} q^2}.$$
 (5.2.1.5)

The relaxation time  $\tau(q)$  depends on the dominant mass transport mechanism involved in the relaxation process of the island shape. There are three limiting mass transport cases [26, 71-73]: When the mass transport is dominated by terrace diffusion and simultaneously terrace diffusion is fast, the relaxation time is given by

$$\tau(\mathbf{q}) = \frac{\mathbf{k}_{\mathrm{B}} \mathbf{T}}{\Gamma_{\mathrm{a}} \widetilde{\mathbf{\beta}}} \mathbf{q}^{-2}. \tag{5.2.1.6}$$

 $\Gamma_a$  is the hopping coefficient and is equal to the inverse of the mean time between two detachment processes of atoms from kink sites onto the terrace [75]. For slow terrace diffusion,  $\tau(q)$  is given by

$$\tau(\mathbf{q}) = \frac{k_{\mathrm{B}}T}{2D_{\mathrm{t}}c_{\mathrm{t}}\tilde{\beta}}\mathbf{q}^{-3},\tag{5.2.1.7}$$

where  $c_t$  and  $D_t$  are the equilibrium adatom concentration per terrace site and the tracer diffusion constant on the terrace, respectively. When the dominant mass transport is edge diffusion, one finds

$$\tau(q) = \frac{k_B T}{\Gamma_h \tilde{\beta}} q^{-4}. \tag{5.2.1.8}$$

Here,  $\Gamma_h$  is the hopping coefficient, which is the inverse of the mean time between two hopping processes along the step edge (save for atom in next-neighbor interactions model) [71]

$$\Gamma_{\rm h} = \Gamma_0 e^{-\frac{E_{\rm act}}{k_{\rm B}T}},\tag{5.2.1.9}$$

where  $E_{act}$  is the activation energy of  $\Gamma_h$ . By using equations (5.1.2.6) – (5.1.2.8) and the definition of q in equation (5.2.1.2), one obtains

$$\tau \propto L_y^{\delta}$$
,  $\delta = 2.3.4$  for the three limiting cases, respectively. (5.2.1.10)

L<sub>y</sub> is limited by the cluster size and the cluster area A<sub>cl</sub>,

$$A_{cl} \propto L_{v}^{2}$$
. (5.2.1.11)

Hence, for the relaxation time one finds

$$\tau \propto A_{\rm cl}^{\delta/2}. \tag{5.2.1.12}$$

For the case when the diffusion is along the island edge, i.e.  $\delta = 4$ , equation (5.2.1.8) becomes

$$\tau \propto \frac{1}{\Gamma_{\rm h}} A_{\rm cl}^2. \tag{5.2.1.13}$$

In equation (5.2.1.13), we make use of the fact that for not too high and not too low temperatures, i.e.  $k_BT << \epsilon$  ( $\epsilon$  is the kink formation energy) the temperature dependence of  $k_BT/\tilde{\beta}$  is negligible. In particular for steps with high kink density on Cu(100), it was shown experimentally that  $k_BT/\tilde{\beta}$  is temperature independent within the experimental error bars for temperatures up to  $\sim$  330 K [76]. For simplicity, it is also assumed that the pre-exponential factor  $\Gamma_0$  of the tracer diffusion coefficient  $D_{st}$  does not depend on temperature. One should emphasize though that this assumption is not always fulfilled. Using equations (5.2.1.9) and (5.2.1.13) and normalizing the relaxation time by the cluster area yields then

$$\ln \frac{A_{cl}^2}{\tau} \propto \ln \Gamma_0 - \frac{E_{act}}{k_B} \frac{1}{T}.$$
 (5.2.1.14)

Hence, from an Arrhenius plot of  $A_{cl}^2/\tau$  one obtains the activation energy of the dominant mass transport mechanism and the pre-exponential factor.

# 5.2.2 Determination of the dominant mass transport mechanism by analyzing the island coalescence on Cu(100)

In this section, the experimental data on vacancy island coalescence events on Cu(100) is presented. The data is analyzed with regard to the mass transport mechanism which dominates the relaxation of the island shape into the equilibrium shape after two vacancy islands merged. In order to analyze island coalescence events, the merged islands have to be of approximately the same size and the merging process has to proceed via a corner-to-corner contact [77] (see e.g. Fig. 5.2.2.1). As an indicator of the progress of the coalescence process the neck width d as well as the cluster length h were used (Fig. 5.2.2.1). In Fig. 5.2.2.2, the time dependence of the neck width d and the

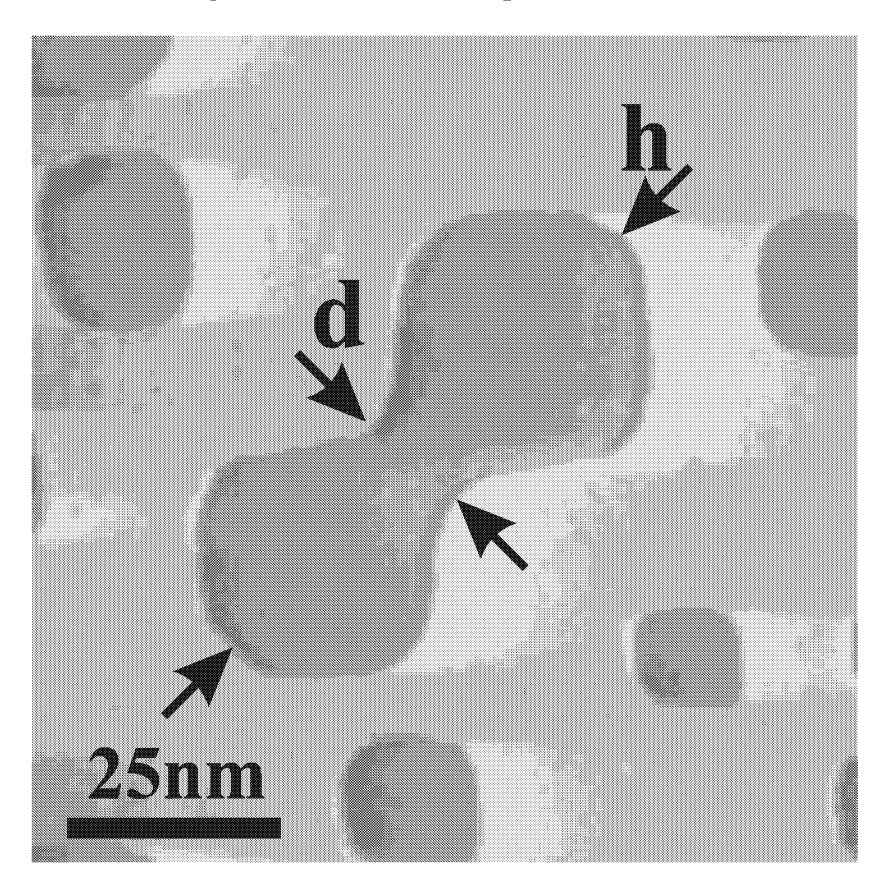


**Figure 5.2.2.1** Definition of the measured neck width d and the cluster length h. STM-image of Cu(100) at 323K, scan width 97.2 nm.

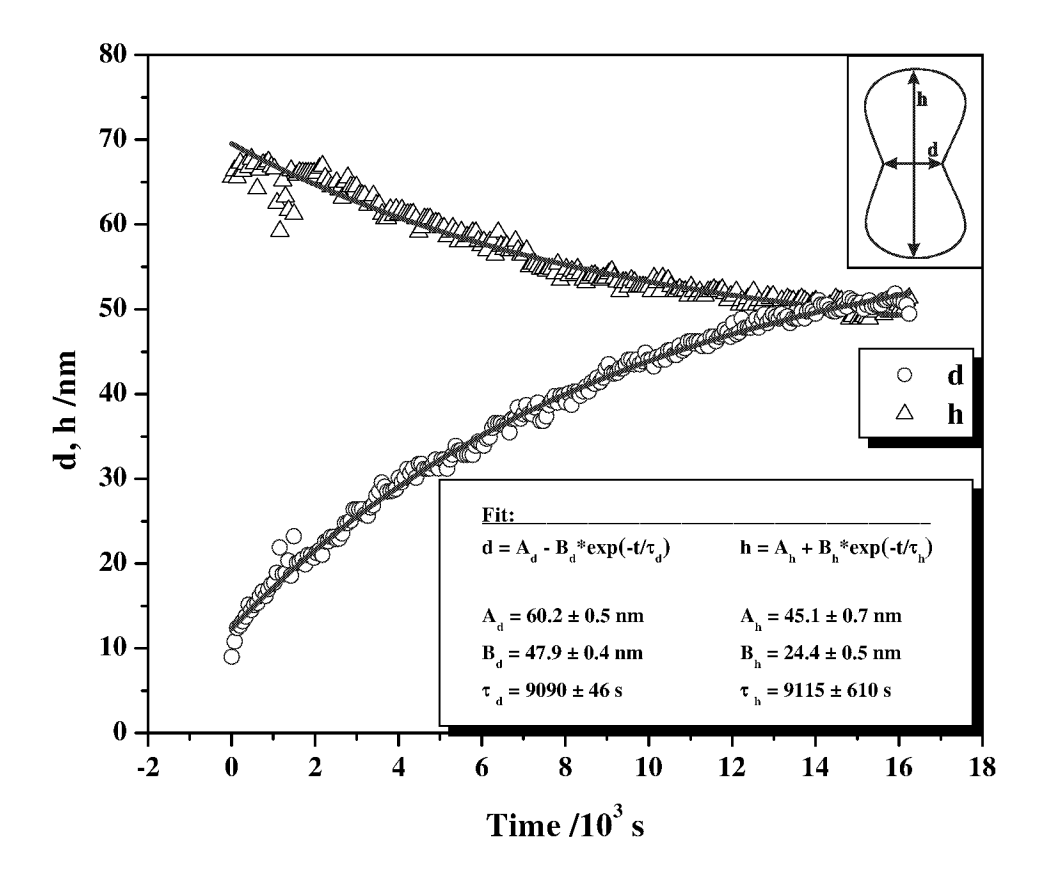


**Figure 5.2.2.2** Time dependence of the neck width d and the largest diameter of the cluster h for the coalesce vacancy islands on Cu(100) at 323K. The experimental data is fitted with exponential functions with free parameters  $A_{d,h}$ ,  $B_{d,h}$  and relaxation times  $\tau_{d,h}$ .

largest cluster diameter h of an island are plotted. The neck width d and the cluster diameter h were measured from the STM images using the same computer program as described in Chapter 3. The time dependencies of d and h are fitted with an exponential

function,  $d = A_d \pm B_d e^{-\frac{t}{\tau_d}}$  and  $h = A_h \pm B_h e^{-\frac{t}{\tau_h}}$ , where  $A_d$ ,  $A_h$  and  $B_d$ ,  $B_h$  and the relaxation times  $\tau_d$ ,  $\tau_h$  are free parameters. In experiment, the relaxation times  $\tau_d$  and  $\tau_h$  determined by the time dependencies of d and h should agree within the error margins. From Fig. 5.2.2.2, one finds  $\tau_d = 9091 \pm 46$  s and  $\tau_h = 9116 \pm 610$  s which is in reasonable agreement. In total, 12 different island coalescence events at 5 different temperatures between T = 303 K and T = 353 K were analyzed. For all of the coalescence events we determined the relaxation time of d and h.

It was shown in the previous section (equation (5.2.1.12)) that the relaxation time depends on the cluster area  $A_{cl}$ . As an example, Fig. 5.2.2.3 shows a log-log plot of

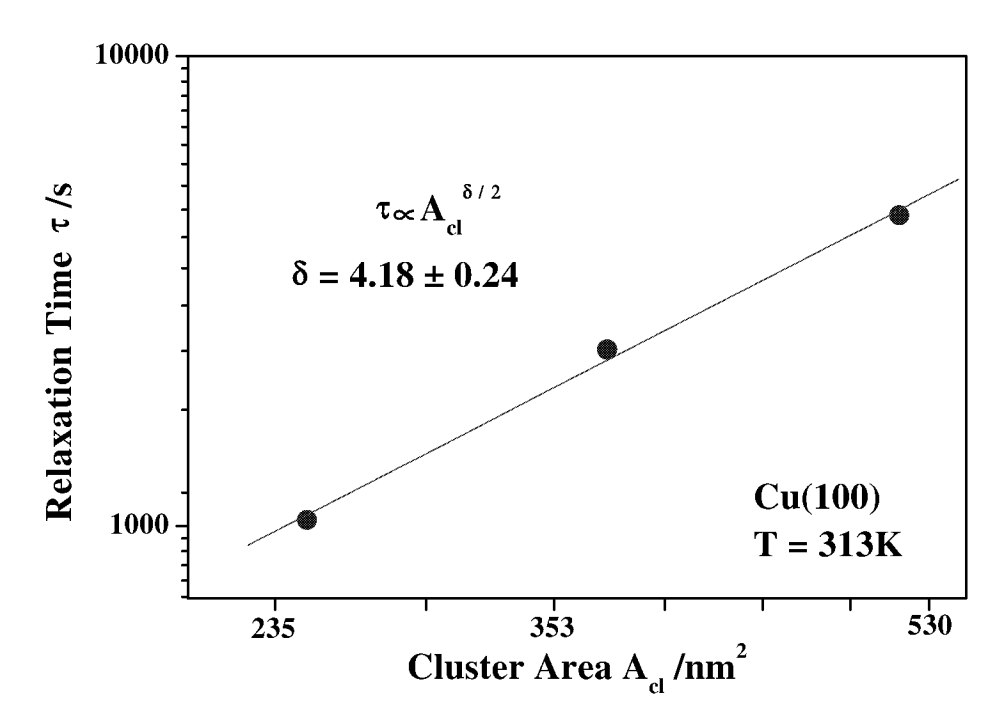


**Figure 5.2.2.3** Log-log plot of the relaxation time vs. cluster area. The slope of the fitting curve is of about 2 which corresponds to  $\delta = 4$ , and hence, diffusion along the island perimeter.

the relaxation time of the neck width d versus the area of three clusters with different area  $A_{cl}$  at 313 K. The solid line is a linear fit to the data and from the slope one obtains the exponent  $\delta$  to be  $\delta \cong 4$ , i.e. the relaxation of the island shape is dominated by periphery diffusion of atoms along the island edge (equation (5.2.1.8)). For all studied coalescence processes in the temperature regime between 303 K and 353 K, we find  $\delta$  to be close to 4. Hence, the mass transport during island coalescence on Cu(100) between 303 K and 353 K is dominated by diffusion along the island edge.

According to equation (5.2.1.14), the relaxation time depends on the temperature. From the temperature-variable STM-studies of island coalescence on Cu(100) between 303K and 353K, one can also determine the activation energy for the diffusion along the island edges. The measured relaxation times for d and h for all observed coalescence events are displayed in the Arrhenius plot in Fig. 5.2.2.4. The results of the measured values of  $\tau$  extracted from the analysis of the neck width d are plotted as circles. The error bars are so small that they fall within the plotted symbol. Data points displayed as squares were obtained from the analysis of the relaxation time

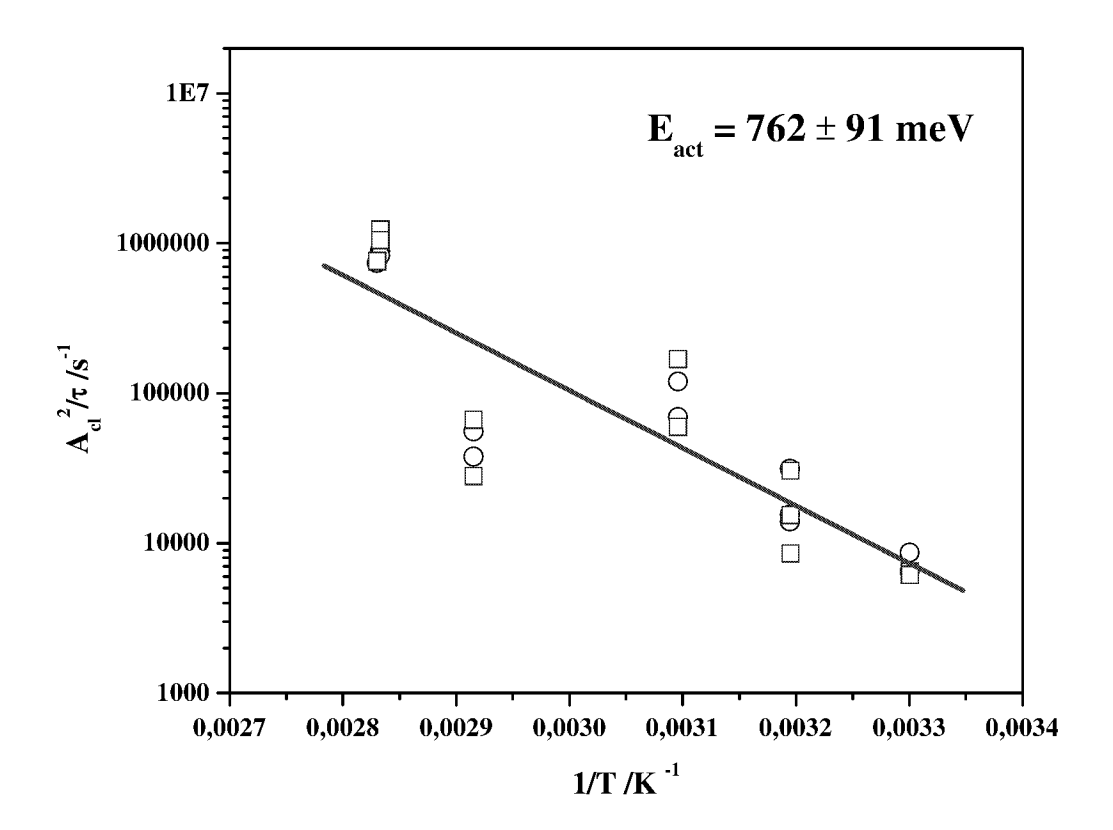


**Figure 5.2.2.4** Arrhenius plot of the normalized relaxation time (equation (5.2.1.14)). The slope of the fit is proportional to the activation energy.

of the cluster diameter h. The solid line is a linear fit to the experimental data. From the slope of the fitting line one finds the activation energy for the diffusion along the island edge to be  $E_{act} = 0.76 \pm 0.09$  eV and pre-exponential factor  $\Gamma_0 = 10^{15 \pm 2}$  s<sup>-1</sup>.

Pai et al [59] discussed STM investigations of island diffusion and coarsening on Cu(100) at room temperature. They showed that the dominant atomic hopping process is diffusion along the island edges which is in agreement with this work. In STM studies of equilibrium fluctuations of infinite steps, Giesen-Seibert et al. could show that between 300 and 370 K the step fluctuations are dominated by edge diffusion [78] in accordance with all experimental results so far. Furthermore, they could give a very accurate value of the activation energy of the step fluctuations of 0.324 eV. Recalculation of this value to the activation energy of the hopping constant  $\Gamma_h$  would give  $E_{act} \approx 0.9$  eV which is significantly larger than the activation energy obtained from

the analysis of the island coalescence. This deviation is quite surprising and cannot be explained easily. One possible solution to the problem could be the use and the interpretation of the hopping constant  $\Gamma_h$ . In the original derivation of the theory for step fluctuations, as described in this work in equations (5.2.1.1) - (5.2.1.8),  $\Gamma_h$  is defined for a step oriented along the atomically dense (110)-direction. That is, the step is almost straight with a low kink density. In that case, the activation energy of  $\Gamma_h$  can be interpreted as the sum of the adatom creation energy from kink sites onto step sites E<sub>ad</sub><sup>st</sup> and the diffusion barrier along a kinked step  $E_d^k$ . For low kink concentrations, the latter energy can be written as the sum of the diffusion barrier along a straight step and the kink formation energy [78]. Then, indeed, one would find an activation barrier for  $\Gamma_h$  of 0.9 eV as mentioned before. The discrepancy between the new data and the previous data on the activation energy seems to indicate that this interpretation of  $\Gamma_h$  is not valid in the case of step edges with a high kink density as is the case for island edges in the neck region after island coalescence. In the center of the neck region indeed, the step is approximately oriented along the  $\langle 100 \rangle$ -direction, i.e. the step has a kink density of 100%. Then, it would be reasonable to assume that the splitting of the activation energy of  $\Gamma_h$  into  $E_{ad}^{st}$  and  $E_d^k$  may not be valid any more. Furthermore, one should keep in mind that the energies  $E_{ad}^{st}$  and  $E_{d}^{k}$  themselves may considerably deviate from those obtained for the quasi-straight step. Therefore, it would be interesting to investigate step fluctuations of steps with high kink density and determine the activation energy of the fluctuations for comparison with the result presented here. A preliminary, however, not very accurate study was recently reported by Giesen and Dieluweit [79] where it was shown that the activation energy of  $\Gamma_h$  for highly kinked steps seems to be about 0.6-0.7 eV, which is much lower than 0.9 eV as found for the quasi-straight steps. The result by Giesen and Dieluweit is in excellent agreement with the measured activation energy of 0.76 eV found in the work presented here. Giesen and Dieluweit gave also an estimate for the pre-exponential factor of  $\sim 10^{21 \pm 1} \, \mathrm{s}^{-1}$ . From the island coalescence we obtain  $\Gamma_0$  $\sim 10^{15 \pm 2} \text{ s}^{-1}$  which is in agreement with the general result that pre-exponential factors are of the order of  $\sim 10^{13} \text{ s}^{-1}$  [80]. However, the result for  $\Gamma_0$  as found here is much lower than the value recently found by Giesen and Dieluweit [79]. Hence, this work

corroborates the conclusion that the hopping coefficient  $\Gamma_h$  has a different microscopic meaning for highly kinked steps compared to steps with a mean orientation along the atomically dense direction.

76 \_\_\_\_\_ Chapter 5

# Summary and outlook

This work focused on the morphology and dynamics of two-dimensional islands on crystal surfaces. Studies on the equilibrium shape of islands, on island shape fluctuations, on island decay, on the fast island decay as well as on island coalescence processes were presented. The first part of the work dealt with islands in equilibrium, with the temperature dependence of the island equilibrium shape as well as with the island fluctuations. The equilibrium shape of islands on Pt(111) was studied in a temperature regime between 533K and 713K. The difference in the step free energies for A- and B-steps on Pt(111) enforce the islands to assume the shape of truncated triangles. With increasing temperature, the island shape gets rounder and the ratio of the local radii to A- and B-steps slightly decreases. From the analysis of island shape fluctuations on Pt(111), absolute values for the step free energies could be determined in experiment for the first time. The analysis of island shape fluctuations to measure absolute step free energies is a relatively new method. In this work, it is demonstrated for the first time that it can be applied to islands with pronounced triangular symmetry as is the case for Pt(111). The values obtained for the step free energies are  $a_{\parallel}\beta_A$ =0.359 eV and  $a_{\parallel}\beta_{B}=0.340$ eV. The derived results are in agreement with recent LDA calculations.

In the second part of the work, the investigation of various dynamic processes on crystal surfaces is addressed. It was demonstrated that studies of non-equilibrium phenomena on a microscopic scale enable the determination of the basic energy barriers and of the dominant mass transport mechanisms on metal surfaces. In particular, the decay of monolayer deep vacancy islands on Cu(100) was investigated. It was shown that the decay of vacancy islands on Cu(100) is diffusion limited which is evident for the fact that mono-vacancies are the dominant transport species on Cu(100) surfaces

rather than adatoms. This conclusion confirms previous studies of adatom island decay on Cu(100) where the decay curves indicated that the island decay is detachment limited. From the temperature dependence of the decay rate we derived the activation energy of the decay of vacancy islands on Cu(100) to be  $E_{vac}+E_{diff}=0.73 eV$ . Comparing this value with previous data one may estimate the attachment barrier of monovacancies at the island edges to be of the order of 0.1 eV. In the future, it would be interesting to investigate whether the mass transport via mono-vacancies is a general phenomenon on fcc(100) surfaces. Despite of the fact that the Ostwald-ripening theory was initially derived for two concentric islands, the decay of a vacancy islands in the terrace surrounded by other vacancy islands is also well described by the Ostwald theory: the time exponent of the decay was found to be about 0,66 which is predicted by the theory.

The rapid island decay is a new, recently observed coarsening phenomenon which attracted quite some interest in the last few years. Rapid island decay is a process, which provides a new very fast channel of mass transport on crystal surfaces. In this work, it is demonstrated for the first time that rapid island decay occurs on Pt(111). The critical distance between island and step edges at which the process sets in was determined to be around 10.49 Å. However, for Pt(111), the rapid island decay process is not as frequent as on Cu(111) and Ag(111) studied previously. This may be due to the higher cohesive energy of Pt(111) which caused even rapid decay events to proceed relatively slow compared to the observation on the Cu(111) and Ag(111) in the considered temperature regime. The rareness of the event made the quantitative analysis of fast island decay quite difficult compared to the previous studies on Ag(111) and Cu(111). In general fast decay event could only be identified after analyzing the decay curves of the islands which made the finding of the rapid island decay events in STM movies a real challenge for Pt(111). Due to the lack of large statistics, it could not be investigated whether the rapid decay events observed on Pt(111) are in agreement with the recently proposed microscopic models of the decay process. Therefore, comprehensive calculations and simulations in which the experimental decay curves are compared with the microscopic model have to be left to the future work. Furthermore, it would be useful to perform STM measurements of rapid island decay on Pt(111) at different temperatures in the future to derive information on the temperature

dependence of the critical distance  $w_c$  and maybe on the activation barrier of the rapid decay process.

In the last part of the work, it was shown that island coalescence is an important coarsening mechanism on Cu(100). The main transport mechanism during the island coalescence on Cu(100) could be determined to be edge diffusion. We measured the activation energy of the process  $E_{act}$  to be  $0.61 \pm 0.09$  eV which is in good agreement with previous results obtained in studies on equilibrium fluctuations of infinite highly kinked steps on Cu(100) vicinal surfaces.

Due to the large number of STM images that had to be analyzed, the developing of a new island edge detection program was necessary. The program described in this thesis makes the island analysis in STM images considerably faster.

Last but not least, it should be emphasized that STM studies of surface dynamical processes have been proven to be useful to extract detailed information on atomic processes and their activation barriers. Using continuum models in order to analyze atomic processes provides the possibility to overcome the problem of the finite scan speed of the STM and that surface diffusion processes at high temperatures are much faster than even the fastest STMs ever may be. In that sense, the STM may be helpful in future for the understanding of nano-structures on surfaces and, hence, for the development of new nano-technologies.

80 \_\_\_\_\_\_ Chapter 6

References 81

# References

[1] Müller E.W., Tsong T.T., Field Ion Microscopy Principles and Applications Elsevier, New York, (1969).

- [2] Binning G, Rohrer H, Helv. Phys. Acta, **57** (1982) 726.
- [3] Binning G., Rohrer H., Gerber C., E. Weibel, Phys. Rev. Lett., **40** (1982) 57.
- [4] Schlößer D.C., *PhD Thesis*, *RWTH Aachen*, *published as report of the Research Center Jülich*, Jül-3475, (1997).
- [5] Schlößer D.C., Verheij L.K., Rosenfeld G., Comsa G., Phys. Rev. Lett., **82** (1999) 3843.
- [6] Steimer C., Giesen M., Verheij L., Ibach H., Phys. Rev. B, **64** (2001) 085416.
- [7] Steimer J.C., *PhD Thesis*, *RWTH Aachen*, *published as report of the Research Center Jülich*, Jül-3862, (2001).
- [8] Khare S.V., Einstein T.L., Phys. Rev. B, **54** (1996) 11752.
- [9] Giesen M., Prog. Surf. Sci., **68** (2001) 1.
- [10] Giesen M., Ibach H., Surf. Sci., **464** (2000) L697.
- [11] Burton W.K., Cabrera N., Frank F.C., Trans. R. Soc. London Ser. A, **243** (1951) 299.
- [12] Desjonquéres M.-C., Spanjaard D., in *Springer Series in surface science*, edited by Gomer R., Mills D.L. Springer Berlin, Vol. 30, p. 15.
- [13] Ehrlich G., Hudda F.G., J. Chem. Phys., 44 (1966) 1039.
- [14] Schwoebel R.L., Shipsey E.J., J. Appl. Phys., **37** (1966) 3682.
- [15] Besocke K., Surf. Sci., **181** (1987) 145.
- [16] Frohn J., Wolf J.E., Besocke K., Teske M., Rev. Sci. Instrum., **60** (1989) 1200.
- [17] Icking-Konert G.S., *PhD Thesis*, *RWTH Aachen*, *published as report of the Research Center Jülich*, Jül-3588, (1998).
- [18] Michely T., Comsa G., Surf. Sci., **256** (1991) 217.
- [19] Girard J.C., Samson Y., Gauthier S., Rousset S., Klein J., Surf. Sci., **302** (1994) 73.
- [20] Icking-Konert G.S., Giesen M., Ibach H., Phys. Rev. Lett., **83** (1999) 3880.
- [21] Lapujoulade J., Surf. Sci. Rep., **20** (1994) 191.

References

- [22] Gorse D., Lapujoulade J., Surf. Sci., **162** (1985) 847.
- [23] Wortis M., in *Springer Series in Surface Science*, edited by Vanselow R., Howe R. Springer Berlin, Vol. 10, p. 367.
- [24] Wulf G., Z. Kristallogr. Mineral., **34** (1901) 449.
- [25] Herring C., Phys. Rev., **82** (1951) 87.
- [26] Khare S.V., Einstein T.L., Phys. Rev. B, **57** (1998) 4782.
- [27] Feibelman P.J., Nelson J.S., Kellogg G.L., Phys. Rev. B, **49** (1994) 10548.
- [28] Feibelman P.J., Phys. Rev. Lett., **81** (1998) 168.
- [29] Feibelman P.J., Phys. Rev. B, **60** (1999) 4972.
- [30] Feibelman P.J., Surf. Sci., **463** (2000) L661.
- [31] Boisvert G., Lewis L.J., Scheffler M., Phys. Rev. B, **57** (1998) 1881.
- [32] Nelson R.C., Einstein T.L., Khare S.V., Rous P.J., Surf. Sci., **295** (1993) 462.
- [33] Herring C., The Use of Classical Concepts in Surface Energy Problems University of Chicago Press, (1953).
- [34] Herring C., Surface Tension as a Motivation for Sintering McGraw-Hill, (1951).
- [35] Icking-Konert G.S., Giesen M., Ibach H., Surf. Sci., **398** (1998) 37.
- [36] Lifshitz L.M., Slyozov V.V., J. Phys. Chem. Solids, **19** (1961) 35.
- [37] Wagner C., Z. Elektrochem., **65** (1961) 581.
- [38] Chakraverty B.K., J. Phys. Chem. Solids, **28** (1967) 2401.
- [39] Wynblatt P., Gjostein N.A., Prog. Surf. Sci., 9 (1975) 21.
- [40] Hannon J.B., Klünker C., Giesen M., Ibach H., Bartelt N.C., Hamilton J.C., Phys. Rev. Lett., **79** (1997) 2506.
- [41] Klünker C., Hannon J.B., Giesen M., Ibach H., Boisvert G., Lewis L.J., Phys. Rev. B, **58** (1998) R7556.
- [42] Karimi M., Tomkowski T., Vidali G., Biham O., phys. Rev. B, **52** (1995) 5364.
- [43] Merikoski J., Vattulainen I., Heinonen J., Ala-Nissila T., Surf. Sci., **387** (1997) 167.
- [44] Giesen M., Icking-Konert G.S., Ibach H., Phys. Rev. Lett., **80** (1998) 552.
- [45] Giesen M., Icking-Konert G.S., Ibach H., Phys. Rev. Lett., **82** (1999) 3101.
- [46] Morgenstern K., Rosenfeld G., Comsa G., Lægsgaard E., Basenbacher F., Phys. Rev. Lett., **85** (2000) 468.

References 83

[47] Morgenstern K., Rosenfeld G., Comsa G., Sørensen M., Hammer B., Lægsgaard E., Phys. Rev. B, **63** (2001) 045412.

- [48] Giesen M., Surf. Sci., **441** (1999) 391.
- [49] Kunkel R., Poelsema B., Verheij L., Comsa G., Phys. Rev. Lett., **65** (1990) 733.
- [50] van der Vegt H.A., van Pinxtern H.M., Lohmeier M., Vlieg E., Phys. Rev. Lett.,68 (1992) 3335.
- [51] Vrijmoeth J., van der Vegt H.A., Meyer J.A., Vlieg E., Behm R.J., Phys. Rev. Lett., **72** (1994) 3843.
- [52] Tsui F., Wellman J., Uher C., Clarke R., Phys. Rev. Lett., **76** (1996) 3164.
- [53] Wulfhekel W., Lipkin N., Kliewer J., Rosenfeld G., Jorritsma L., Poelsema B., Comsa G., Surf. Sci., **348** (1996) 227.
- [54] Li J., Schneider W.-D., Berndt R, Crampin S., Phys. Rev. Lett., **80** (1998) 3332.
- [55] Kevan S.D., Phys. Rev. Lett., **50** (1983) 526.
- [56] Kevan S.D., Gaylord R.H., Phys. Rev. B, **36** (1987) 5809.
- [57] Bartelt N.C., private communication, (1997).
- [58] Zuo J.-K., Wendelken J.F., Dürr H., Liu C.-L., Phys. Rev. Lett., **72** (1994) 3064.
- [59] Pai W.W., Swan A.K., Zhang Z., Wendelken J.F., Phys. Rev. Lett., 79 (1997)3210.
- [60] Wen J.M., Evans J.W., Bartelt M.C., Burnett J.W., Thiel P.A., Phys. Rev. Lett.,76 (1996) 652.
- [61] Cadilhe A.M., Stoldt C.R., Jenks C.J., Thiel P.A., Evans J.W., Phys. Rev. B, **61** (2000) 4910.
- [62] Hoogeman M.S., Klik M.A.J., van Castel R., Frenken J.W.M., J. Phys.: Condens. Matter, 11 (1999) 4349.
- [63] Eßer M., Morgenstern K., Rosenfeld G., Comsa G., Surf. Sci., **402-404** (1998) 341.
- [64] Rosenfeld G., Morgenstern K., Esser M., Comsa G., Appl. Phys. A, **69** (1999) 489.
- [65] von Smoluchowski M., Physik. Zeitschr., **17** (1916) 585.
- [66] von Smoluchowski M., Z. Phys. Chem., **92** (1917) 129.
- [67] Meakin P., Physica A, **165** (1990) 1.
- [68] Mullins W.W., J. Appl. Phys., **30** (1959) 77.

References References

[69] Nichols F.A., Mullins W.W., Transaction of Metallurgical Society of AIME, **233** (1965) 1840.

- [70] Khare S.V., Bartelt N.C., Einstein T.L., Phys. Rev. Lett., **75** (1995) 2148.
- [71] Bartelt N.C., Einstein T.L., Williams E.D., Surf. Sci., **312** (1994) 411.
- [72] Jeong H.-C., Williams E.D., Surf. Sci. Rep., **34** (1999) 171.
- [73] Blagojevic B., Duxbury P.M., Phys. Rev. E, **60** (1999) 1279.
- [74] Noziéres P., in *Solids Far From Equilibrium*, edited by Godréche C. Cambrige University Press, (1991), p. 1.
- [75] Bartelt N.C., Goldberg J.L., Einstein T.L., Williams E.D., Surf. Sci., **273** (1992) 252.
- [76] Dieluweit S., Ibach H., Giesen M., Einstein T.L., Phys. Rev. B, **67** (2003) 121410(R).
- [77] Stoldt C.R., Cadilhe A.M., Jenks C.J., Wen J.-M., Evans J.W., Thiel P.A., Phys. Rev. Lett., 81 (1998) 2950.
- [78] Giesen-Seibert M., Schmitz F., Jentjens R., Ibach H., Surf. Sci., 329 (1995) 47.
- [79] Giesen M., Dieluweit S., J. Molec. Cat., (in press)
- [80] Kellogg G.L., Surf. Sci. Rep., 21 (1994) 1.

# Acknowledgments

I want first of all say thanks ever so much to my doctoral advisor Mrs. Dr. Margret Giesen, who guided me through the thesis at the Institut für Schichten und Grenzflächen (ISG). Her talent of comprehensible explaining the physical basics of the microscopic processes involved in the surface diffusion phenomena that we investigated will ever amaze me. I thank her for the support, the understanding and the patience in the hard times during my work. Without her advice and help this thesis will not have been the same.

Many thanks also to Prof. Dr. Harald Ibach for the precise advices that he gave me with respect to the critical points in the analysis of the experimental data. I thank him also for the possibility to make this PhD thesis in the friendliest team of the ISG. At this point I should also not forget to thank Prof. Dr. R. Merkel who gave us a new scientific home and financial support since our transfer from the ISG 3 to ISG 4.

I am especially grateful to Dr. Kirilka Starbova and Dr. Nikolay Starbov for the efficient assistance in my experimental work and to Mr. Karl Hieble for the technical 'tips and tricks'. The large number of measurements provided for this thesis will not have been possible without their help.

Special gratitude also to Dr. Sabine Dieluweit for enjoyable and productive discussions and her help in the development of my German language skills. Thanks to Ernesto Pichardo-Pedrero for the pleasant talks.

I am much obliged to Mr. Udo Linke for the excellently prepared platinum and copper crystals, which were very important for the proper proceeding of the experimental work.

To all the colleagues in ISG-3 and ISG-4, whom I did not mentioned above personally, I address my thankfulness and gratitude.

I want also to say "Thank you" to my parents and my brother who steadily support me and somehow endure my absence from home.

Last but not least special gratitude to Ekaterina Foteva. She stood by me all the time and supported me when I needed it. Thank you!



Jül-4144 August 2004 ISSN 0944-2952